

The Description and Validation of a Computationally-Efficient CH₄-CO-OH (ECCOHv1.01) Chemistry Module for 3D Model Applications

Elshorbany, Yasin F.^{1,2*}, Duncan, Bryan N.¹, Strode, Sarah A.^{1,3}, Wang, James S.^{1,3}, Kouatchou, Jules^{1,4}

¹NASA Goddard Space Flight Center, Greenbelt, Maryland, USA

²Earth System Science Interdisciplinary Center, University of Maryland, College Park, Maryland, USA

³Universities Space Research Association, Columbia, Maryland, USA

⁴Science Systems and Applications Inc., Lanham, Maryland, USA

*Correspondence to: Y. F. Elshorbany (yasin.f.elshorbany@nasa.gov)

Abstract:

We present the Efficient CH₄-CO-OH chemistry module (ECCOH) that allows for the simulation of the methane, carbon monoxide and hydroxyl radical (CH₄-CO-OH) system, within a chemistry climate model, carbon cycle model, or earth system model. The computational efficiency of the module allows many multi-decadal sensitivity simulations of the CH₄-CO-OH system, which primarily determines the global atmospheric oxidizing capacity. This capability is important for capturing the nonlinear feedbacks of the CH₄-CO-OH system and understanding the perturbations to methane, CO and OH and the concomitant impacts on climate. We implemented the ECCOH chemistry module into the NASA GEOS-5 Atmospheric Global Circulation Model (AGCM), performed multiple sensitivity simulations of the CH₄-CO-OH system over two decades, and evaluated the model output with surface and satellite datasets of methane and CO. The favorable comparison of output from the ECCOH chemistry module (as configured in the GEOS-5 AGCM) with observations demonstrates the fidelity of the module for use in scientific research.

1 Introduction

The coupled methane - carbon monoxide - hydroxyl radical (CH₄-CO-OH) system is nonlinear (e.g., Prather, 1994) and important in determining the atmosphere's oxidizing capacity (e.g., Chameides et al., 1976). Methane is the second most important anthropogenic greenhouse gas (GHG), though its 100-year global warming potential (GWP) is 34 times larger than that for carbon dioxide (CO₂; Myhre et al., 2013). Methane is responsible for about 20% of the warming induced by long-lived GHG's since pre-industrial times (Kirschke et al., 2013). The CH₄-CO-OH system has implications for tropospheric ozone and, subsequently, air quality (e.g., Fiore et al., 2002). A thorough understanding of historical methane, CO and OH trends and variations is necessary to credibly predict future changes and their climate feedback, as well as, to develop strategic national and international emission reduction policies.

The major limitation of forward modeling studies of trends and variability in the CH₄-CO-OH system is the computational expense associated with simulating ozone-nitrogen oxides-volatile organic compounds (O₃-NO_x-VOC) photochemistry for the determination of OH, particularly since perturbations to relatively long-lived methane (~8-10 y) can take several

42 decades to fully evolve (e.g., Prather, 1996). There are few forward modeling studies in the
43 literature that carry a full representation of O₃-NO_x-VOC chemistry, and they necessarily
44 present a limited number of sensitivity simulations (e.g., Fiore et al., 2006; Voulgarakis et
45 al., 2015).

46 To overcome this computational expense, global modeling communities often use archived
47 and annually-repeating monthly OH fields to simulate the oxidation of methane and CO. In
48 the TransCom methane model intercomparison project (MIP), archived and annually-
49 repeating OH fields were used from a climatology (Spivakovsky et al., 2000). Wang et al.
50 (2004) used archived and annually-varying OH fields from Duncan et al. (2007a) to explain
51 the causes of observed interannual variations in methane and the observed slowdown in its
52 growth rate from 1988 to 1997.

53 Limitations of using archived, monthly OH fields for studies of methane's and CO's
54 evolution are that feedbacks of the CH₄-CO-OH system on methane, CO and OH are not
55 captured as the losses of methane and CO by reaction with OH are assumed to be linearly
56 proportional to the OH fields. For methane, this assumption is not desirable, particularly on
57 multi-decadal time-scales (e.g., Prather, 1996). Chen and Prinn (2006) found that using an
58 archived, annual cycle of OH may mask or bias the interannual changes of methane. For
59 relatively short-lived CO (~1-2 months), this assumption is not valid given the strong
60 feedback between CO and OH (e.g., Duncan and Logan, 2008; Voulgarakis et al., 2015). If a
61 multi-decadal simulation of methane or CO using archived and annually-repeating OH
62 reproduces observations, then there must be some compensating factor, for example a bias in
63 emissions. That is, the simulation reproduces observations, but for the wrong reason. The
64 models in the TranCom MIP adjusted down (by 8%) the archived OH climatology of
65 Spivakovsky et al. (2000) so that the simulated decline in the global, atmospheric
66 methylchloroform (MCF) concentration since 2000 better matched that observed (Patra et al,
67 2011). Adjusting archived OH to improve a simulation of MCF, methane and/or CO makes
68 the specious assumption that emissions inventories, model dynamics, etc. used in the
69 simulation are correct. If using archived and annually-repeating OH, whether adjusted or
70 not, inverse modeling studies of methane and CO will incorrectly determine a posteriori
71 fluxes as the impact of nonlinear feedbacks of the CH₄-CO-OH system on concentrations
72 will be erroneously folded into the flux estimates. Therefore, there is a need for a
73 computationally-efficient solution to simulate credible temporal and spatial distributions of
74 OH over several decades, while capturing the nonlinear feedbacks of the CH₄-CO-OH
75 system.

76 In this manuscript, we present and validate the new, computationally-Efficient CH₄-CO-
77 OH (ECCOH; pronounced like "echo") chemistry module to interactively simulate the
78 chemistry of the CH₄-CO-OH system within a chemistry-climate model, carbon cycle model,
79 or Earth System Model. The computational efficiency of the ECCOH chemistry module
80 allows many sensitivity simulations of multiple decades to be performed, which is important
81 for capturing the nonlinear feedbacks of the CH₄-CO-OH system and understanding the
82 perturbations to methane and the concomitant impacts on climate. The ECCOH chemistry
83 module allows one to deconvolve the impacts of various causal factors (e.g., overhead ozone
84 column, NO_x, VOCs, water vapor, etc.) on OH and, subsequently, on methane and CO.
85 Therefore, this capability is valuable in determining these impacts, especially, given that

86 simulated OH varies widely between models (Shindell et al., 2006; Fiore et al., 2009) for a
87 variety of reasons, including differences in the causal factors that influence OH (Shindell et
88 al., 2006). For instance, Voulgarakis et al. (2013) found that simulated tropospheric methane
89 lifetimes of various models ranged from ~7 to ~14 years; this spread is similar to that
90 calculated by Shindell et al. (2006) and Fiore et al. (2009), even when all participating
91 models used identical methane abundances and CO emissions (Shindell et al., 2006).
92 Shindell et al. (2006) related the wide spread of simulated CO between models to the large
93 spread in simulated OH. Furthermore, simulated OH from full chemistry mechanisms in
94 global models is still highly uncertain because of incomplete knowledge and representation
95 of OH sources, sinks and recycling (e.g., Elshorbany et al., 2010, 2012a, 2012b, 2014; Stone
96 et al., 2012). For example, 1) nitrous acid (HONO) is typically underestimated in models by
97 an order of magnitude (Elshorbany et al., 2012b), which can lead to a significant
98 underestimation of OH, especially in urban high-NO_x regions; 2) in unpolluted, forested
99 environments, significant discrepancies exist between models and measurements (Stone et
100 al., 2012); and 3) Patra et al. (2014) indicate that the inter-hemispheric OH ratio (northern to
101 southern hemisphere) is near unity, while a recent model inter-comparison had a multi-model
102 average of about 1.3.

103 The manuscript is organized as follows: In Sect. 2, we 1) describe the ECCOH chemistry
104 module as implemented in the NASA Goddard Earth Observing System, Version 5
105 Atmospheric General Circulation Model (GEOS-5 AGCM), and 2) and describe a series of
106 simulations, which we refer to as “scenarios” hereafter, to illustrate the utility of the ECOOH
107 module for understanding the influence of various factors on the observed spatial
108 distributions and temporal evolution of methane, CO, and OH. In Sect. 3, we show that the
109 simulated trends and variations of methane and CO in our reference scenario agree well with
110 in situ and satellite measurements. In Sect. 4, we demonstrate the ability of the ECCOH
111 chemistry module to capture the nonlinear chemistry of the CH₄-CO-OH system with output
112 from our sensitivity scenarios.

113 **2 Technical Approach and Methodology**

114 **2.1 Description of the ECCOH Chemistry Module and Its Implementation**

115 The ECCOH chemistry module is composed of a parameterization of tropospheric OH and
116 tracers of methane and CO as shown in Fig. 1. The advantage of the ECCOH chemistry
117 module over a full representation of O₃-NO_x-VOC chemistry is computational
118 efficiency. The computational cost of simulating tropospheric OH is reduced by about a
119 factor of 500 when the full O₃-NO_x-VOC chemistry is replaced by the parameterization of
120 OH (Duncan et al., 2000). This computationally-efficient parameterization of OH allows 1)
121 for many multi-decadal model sensitivity simulations to be performed and 2) one to
122 deconvolve the impact of various factors on the observed trends and variability in methane
123 and CO. It is based on the method described by Spivakovsky et al. (1990a), who developed
124 an earlier version of the parameterization of OH used in several studies, including
125 Spivakovsky et al. (1990b) and Prather and Spivakovsky (1990). The parameterization of
126 OH of Duncan et al. (2000) is designed to simulate OH over the range of photochemical
127 environments found throughout the troposphere, including a wide enough range so as to be

128 applicable to preindustrial, present day and possible future conditions (Duncan et al., 2000).
129 It has been implemented into two host atmospheric models and has been used in several
130 studies of the nonlinear feedbacks of CO and OH (Duncan et al., 2007a; Duncan and Logan,
131 2008; Strode et al., 2015).

132 The parameterization of OH accurately represents OH predicted by a full chemical
133 mechanism as a set of high-order polynomials that describe the functional relationship
134 between the concentration of OH and meteorological variables (i.e., pressure, temperature,
135 cloud albedo), solar irradiance variables (i.e., ozone column, surface albedo, declination
136 angle, latitude) and chemical variables, including CO and methane as well as nitrogen oxides
137 (as a family), ozone, water vapor, and various VOCs. That is, the 24-hour average OH is
138 calculated interactively in the model and responds to changes in the concentrations of trace
139 gases and meteorology. Input variables to the parameterization of OH may be taken from
140 archived fields from, for instance, an observational climatology or archived fields from a
141 model simulation with a full representation of trace gas and aerosol atmospheric chemistry,
142 and may be annually-repeating or annually-varying. Some variables (e.g., water vapor,
143 clouds) may be taken from the host model as the simulation progresses. Ideally, all input
144 variables should be annually-varying so as to best capture the nonlinear feedbacks of the
145 CH₄-CO-OH system. If one chooses to use output from a single computationally-expensive
146 full chemistry model simulation as input to the parameterization of OH, subsequent
147 sensitivity simulations using the ECCOH chemistry module will be far less computationally-
148 expensive relative to that single expensive simulation, which is the primary strength of using
149 the parameterization of OH. In Section 2.2, we discuss the setup of the simulations presented
150 in this study.

151 We adjust the OH from the parameterization to account for important updates in kinetic
152 information of O¹D reactions by water vapor, molecular nitrogen, and molecular oxygen
153 (Sander et al., 2011). These reactions are key as the primary production pathway (P) for OH
154 involves the formation of excited O¹D atoms by photolysis of ozone (O₃), followed by their
155 reaction with water vapor in competition with their collisional quenching by molecular
156 nitrogen and oxygen: $P = j[\text{O}_3] * 2k_1[\text{H}_2\text{O}] / (k_1[\text{H}_2\text{O}] + k_2[\text{N}_2] + k_3[\text{O}_2])$, where j is the
157 ozone photolysis rate and k_1 , k_2 and k_3 are the rate constants of O¹D reactions with water
158 vapor, nitrogen and oxygen, respectively. Typically, this adjustment decreases OH by 10-
159 30%, depending on altitude and season. Recent updates in isoprene chemistry are not
160 reflected in the parameterization of OH, so OH near the surface in clean, forested
161 environments (e.g., Amazon and Congo basins) is too low relative to current knowledge
162 (e.g., Fuchs et al., 2013). However, the contribution of these regions to global methane and
163 CO loss is small (i.e., < 1%) and the current knowledge of isoprene photochemistry is still
164 highly uncertain (Fuchs et al., 2013). Ultimately, the parameterization of OH reflects
165 uncertainties in the chemistry upon which it is based, as do the photochemical mechanisms
166 in all atmospheric chemistry models (e.g., Stone et al., 2012; Fuchs et al., 2013). The losses
167 of methane and CO in the ECCOH chemistry module are determined by their reaction with
168 tropospheric OH. Additional losses of methane in the stratosphere occur by reactions with
169 OH, Cl and O¹D, whose distributions are simulated using archived and annually-repeating
170 monthly fields.

171 We implemented the ECCOH chemistry module into the Goddard Earth Observing

172 System, Version 5 Atmospheric General Circulation Model (GEOS-5 AGCM, Fortuna
173 version, Rienecker et al., 2008; Pawson et al., 2008; Ott et al., 2010; Molod et al., 2012).
174 The AGCM combines the finite volume dynamical core described by Lin (2004) with the
175 GEOS-5 column physics package, as summarized by Rienecker et al. (2008). The AGCM
176 domain extends from the surface to 0.01 mb and uses 72 hybrid layers that transition from
177 terrain following near the surface to pure pressure levels above 180 mb. We use a horizontal
178 resolution of 2° latitude \times 2.5° longitude and the time step is 30 minutes for physical
179 computations.

180 **2.2 Description of the Reference and Sensitivity Scenarios**

181 To demonstrate the utility of the ECCOH chemistry module for multi-decadal studies, we
182 performed several model simulations using the module in the GEOS-5 AGCM (Table 1 and
183 Table 2). The model setup (i.e., emissions, input to the parameterization of OH, and
184 dynamics) of the reference scenario, which we refer to as the *Base* scenario, is detailed in
185 Table 1. Compared to the sensitivity scenarios described in Table 2, the *Base* scenario is the
186 least complex. For example, all CO emissions and natural methane emissions are for one
187 year that are repeated for each year of the simulation (1988-2007); therefore, interannual
188 variations in methane and CO levels caused by variations in these emissions will not be
189 captured in the *Base* scenario. However, there are two important sources of variability that
190 are included in the *Base* scenario. First, the dynamics are constrained by varying sea surface
191 temperatures and sea ice concentrations. Therefore, the *Base* scenario will capture variations
192 in methane, CO, and OH resulting from meteorological variations, such as those associated
193 with the El Niño Southern Oscillation (ENSO). In addition, atmospheric temperature,
194 pressure and specific humidity are calculated online by the GEOS-5 AGCM and are fed into
195 the parameterization of OH as the runs progress, so interannual variations in water vapor,
196 temperature, and cloud cover are also included in the *Base* scenario. These factors are known
197 to influence variations in OH and thus CO and methane (e.g., Holmes et al., 2013). Second,
198 interannual variations in anthropogenic methane sources are included in the *Base* scenario. In
199 Sect. 3, we evaluate model output from the *Base* scenario with the observational datasets
200 described in Table 3.

201 We present the results of our sensitivity scenarios in Sect. 4. We explore the influence of
202 several causal factors on the observed spatial distributions and temporal evolutions of
203 methane, CO, and OH. These causal factors include annually-varying methane and CO
204 emissions (i.e., Scenarios 2-4 in Table 2; natural methane emissions, and anthropogenic and
205 natural CO emissions, Figs. S1 and S2 in the Supplement) and annually-varying input
206 variables to the parameterization of OH (i.e., Scenario 5 in Table 2).

207 **3 Evaluation of the *Base* Scenario**

208 We evaluate the model output of methane and CO from the *Base* scenario with satellite
209 and in situ observations (Table 3). We also compare simulated OH with that from a GEOS-5
210 AGCM simulation (with a full representation of O₃-NO_x-VOC chemistry (Strode et al.,
211 2015)). We highlight where the *Base* scenario's simplicity results in a poor or satisfactory
212 comparison of the model output with the observed temporal and spatial distributions of

213 methane, CO, and OH. We demonstrate that the ECCOH chemistry module for this scenario
214 reasonably captures the distributions of methane and CO, within the limitations of this
215 scenario, as compared to measurements and other model studies (e.g., Shindell et al. 2006;
216 Patra et al., 2011; Naik et al., 2013).

217 **3.1 Tropospheric OH**

218 There are very few direct observations of OH with which to constrain models (e.g., Stone
219 et al., 2012) and none on regional or global scales. Therefore, the MCF lifetime inferred
220 from measurements serves as a widely used, indirect proxy for global OH abundance (e.g.,
221 Lawrence et al., 2001). Though useful, the MCF lifetime gives an incomplete description of
222 the spatial and vertical distributions of OH (e.g., Lawrence et al., 2001) and there are
223 uncertainties concerning MCF emissions and the resulting lifetime estimate (e.g., Wang et
224 al., 2008). Nevertheless, the MCF data have been recently used to infer the ratio of OH in the
225 Northern to the Southern Hemisphere (Patra et al., 2014).

226 Despite the challenges concerning OH, we show in this section that the spatial and vertical
227 distributions of simulated global mean OH (Fig. 2 and Fig. 3) from the *Base* scenario are
228 reasonable relative to the MCF proxy for OH as well as to simulated OH from other models.
229 Related to the OH dependency on UV radiation (Rohrer and Berresheim, 2006), the
230 maximum and minimum OH levels at any given location occur in local summer and winter,
231 respectively (Fig. 2). OH maximizes around 600 mb because of vertical dependencies of the
232 main sources and sinks of OH (Spivakovsky et al., 1990). The seasonal and vertical
233 distributions of the zonal mean OH in the *Base* scenario are quite comparable to the OH
234 climatology of Spivakovsky et al. (2000; see Figure 6 of Spivakovsky et al.), despite the
235 different inputs given to the parameterization of OH in the two studies.

236 The interannual variations in global OH (given by the annual mean standard deviation, not
237 shown) are small (<5%) and mainly related to meteorological variations (e.g., water vapor,
238 clouds, temperature, and transport) as annually-repeating emissions are used in the *Base*
239 scenario, except for anthropogenic methane emissions (Table 1, Fig. S 1, Fig. S 2). This
240 result is consistent with Voulgarakis et al. (2013) who show that OH has the strongest
241 relationship with changes in temperature and humidity when emissions do not vary
242 interannually. As discussed in Sect. 4, we see considerably larger variations in OH in several
243 of our more complex sensitivity simulations, which have interannual variations in methane
244 and CO emissions as well as in factors that affect OH.

245 Over our simulation period, the range of annual mean, atmospheric MCF lifetimes is
246 6.08 ± 0.60 to 6.53 ± 0.65 years with respect to loss by reaction with tropospheric OH for the
247 *Base* scenario, assuming a MCF uniform mixing ratio. Our lifetimes are similar to values
248 reported in the literature (e.g., $6.0^{+0.5}_{-0.4}$ years (Prinn et al., 2005); multi-model mean of
249 5.7 ± 0.9 years (Naik et al., 2013); 6.3 ± 0.9 years (Prather et al., 2012)). The global, annual
250 mean lifetime of methane with respect to tropospheric OH ranges from 10.10 ± 1.06 to
251 10.86 ± 1.15 years. These values are similar to those inferred from measurements (e.g.,
252 $10.2^{+0.9}_{-0.7}$ years (Prinn et al., 2005)) as well as to those reported in previous multi-model
253 comparison studies (e.g., 9.7 ± 1.7 years (Shindell et al., 2006); 10.19 ± 1.72 years (Fiore et al.,
254 2009); 9.7 ± 1.5 years (Naik et al., 2013)). The lifetime of methane is calculated by dividing

255 the total atmospheric burden by the tropospheric methane loss rate (e.g., Fiore et al., 2009).
256 We also compare our simulated OH with that from a GEOS-5 AGCM simulation that
257 carries a full representation of O₃-NO_x-VOC chemistry. This simulation was included in the
258 Atmospheric Chemistry and Climate Model Intercomparison Project (ACCMIP, Lamarque et
259 al., 2013; the model is designated as “GEOSCCM”). Henceforth, we refer to this simulation
260 as the “ACCMIP simulation”. The same CO emissions (annually-repeating emissions for
261 year 2000) are used in both the *Base* and ACCMIP simulations, but there are differences
262 between the simulations (e.g., model dynamics, prescribed methane, etc.). Despite these
263 differences, we find that the spatial and vertical distributions of OH are quite similar with
264 differences generally less than 10% (Fig. S 17). The global, mean tropospheric OH in the
265 *Base* scenario of 10.9×10^5 molecules cm⁻³ also compares well with that of 11.4×10^5
266 molecules cm⁻³ from the ACCMIP simulation (the 2000 time slice) as well as within the
267 range of means from other models (e.g., $6.5 - 13.4 \times 10^5$ molecules cm⁻³ (Voulgarakis et al.,
268 2013)).

269 3.2 Methane

270 *GMD surface data:* We evaluate our simulated surface distributions of methane with data
271 from the NOAA Global Monitoring Division (GMD) network. The simulated, interannual
272 variation of methane’s global growth rate agrees reasonably well ($R^2 = 0.44$) with that
273 estimated from GMD data, using all available data from 92 stations over the simulation
274 period 1988-2007 (Fig. 4a). The agreement of model output with observations is worse (R^2
275 = 0.33) when we only use the 17 stations that cover the entire simulation period (Fig. 4b).
276 We decided to include all 92 stations, even those without records that cover the entire
277 simulation period, as we are able to nearly reproduce Fig. 4a using 46 stations that have at
278 least 75% data coverage (not shown). A relatively high correlation coefficient ($R^2 = 0.44$)
279 implies that interannual variations in anthropogenic methane emissions and dynamics
280 explain much of methane’s growth rate over the study period, which is consistent with the
281 findings of the TransCom MIP (Patra et al., 2011).

282 Overall, the comparison of model output and data at individual GMD stations is favorable.
283 Fig. 5 to Fig. 7 show comparisons for monthly averages, seasonal averages, and annual
284 differences, respectively, at six GMD stations, which were chosen as they have long time
285 records and cover a wide range of latitudes. Over the simulation period (1988-2007), the
286 correlation slope (S) and coefficient (R^2) for these six stations (Table 4) range from 0.56 to
287 0.79 and from 0.58 to 0.91, respectively.

288 There are two important features of the observations that are not simulated in the *Base*
289 scenario. First, the *Base* scenario overestimates methane concentrations by 20-30 ppbv at
290 the northern high latitude stations of Alert and Barrow during the 1980s and 1990s (Fig. 5-
291 Fig. 7). The overestimation of methane in the northern hemisphere during the 1990s occurs
292 because of regional high biases in natural methane emissions (Fig. S 1 and Patra et al., 2011).
293 As shown in Sect. 4.3, simulated methane improves significantly in the northern hemisphere
294 in the *E_{CH4}Vary* scenario, which includes annually-varying natural methane emissions.
295 Second, the *Base* scenario captures the increasing observed methane trend in the 1990s, but
296 under-predicts methane in the 2000’s (Fig. 7). Both of these features (i.e., high bias at high

297 northern latitudes in the 1990's and low bias in the 2000's) are consistent with the findings
298 of the TransCom MIP that used the same methane emissions (Table 1 and Patra et al., 2011).

299 *SCIAMACHY methane*: We compare the simulated methane dry columns to those from
300 SCIAMACHY (Table 3, Fig. 8). The data have the best global spatial coverage during boreal
301 summer because of lower cloud cover during this season (Schneising et al., 2011). The
302 observed methane dry columns reach their highest levels during boreal summer and fall,
303 maximizing over Asia (eastern China and northern India) because of high emissions from
304 wetlands and rice paddies. The *Base* scenario reproduces the spatial distribution of the data
305 well with a bias of $< 2\%$ over most of the globe, except over eastern Asia and western US
306 during boreal summer where it is biased low, but still within the measurement uncertainties
307 ($\sim 7\text{-}10\%$; Gloudemans et al., 2008; Houweling et al., 2014). Houweling et al. (2014)
308 demonstrate that SCIAMACHY data have a seasonal bias that ranges from about -50 ppb
309 during boreal winter to about $+50$ ppb during boreal summer as compared to the Total
310 Carbon Column Observing Network (TCCON) measurements, which may also explain the
311 simulated seasonal biases (Fig. 8).

312 3.3 CO

313 *GMD surface data*: The *Base* scenario captures the monthly variability of GMD CO data
314 well with a mean correlations slope (S) and coefficient (R^2) of 0.81 and 0.72, respectively
315 (Fig. 9 to Fig. 11, Table 4). This result indicates that the seasonal CO cycle is well captured
316 in the *Base* scenario (Fig. 11), which includes annually-repeating, but seasonally-varying
317 biomass burning emissions (Fig. S 2). As expected, the *Base* scenario does not capture the
318 significant interannual variations associated with strong variations in emissions (Fig. 9, Fig.
319 10). The low biases reach ~ 40 ppb in boreal winter and spring at high northern latitudes.
320 During the 1980's and 1990's, CO levels in the northern hemisphere declined substantially
321 because of changing patterns of emissions (Duncan et al., 2007a), which is not simulated
322 with annually-repeating CO emissions. These results are in agreement with the findings of
323 the multi-model ACCENT study (using annually-repeating CO emissions), in which there
324 was a low bias of ~ 50 ppbv at northern hemisphere high latitude stations (Shindell et al.,
325 2006), as well as with other recent studies (e.g., Monks et al., 2015).

326 *MOPITT and TES/MLS CO*: The primary advantage of satellite data, above ground-based
327 networks, is spatial coverage, so we compare the spatial and seasonal distributions of
328 simulated CO with those from the MOPITT and TES/MLS instruments (Fig. 12, Fig. 13).
329 The distributions of CO from the *Base* scenario compare well overall with the data. The
330 mean biases relative to both datasets are within $\pm 10\%$ over most of the globe and in all
331 seasons. For example, the seasonal correlation slopes (S) range from 0.75 to 0.98 and
332 coefficients (R^2) range from 0.80 to 0.98, respectively, between MOPITT, TES/MLS data
333 and the *Base* scenario output with the agreement generally highest during boreal winter and
334 lowest during boreal summer. However, the largest biases (Fig. 12) occur over 1) tropical
335 and subtropical biomass burning regions ($\sim 20\%$) during boreal winter, indicating that either
336 the CO emissions used in the *Base* scenario are too high or that simulated OH is too low, and
337 2) most of the northern hemisphere ($< -20\%$) during the summer season, indicating that
338 either CO emissions are too low or that OH levels are too high, which is consistent with

339 previous studies using similar emissions (e.g., Shindell et al., 2006; Strode et al., 2015). In
340 addition to possible biases associated with emissions, some of the model-observation
341 discrepancies may be associated with uncertainties in the satellite datasets (Ho et al., 2009;
342 Deeter et al., 2012; Amnuaylojaroen et al., 2014). Based on direct comparison with Tall
343 Tower measurements, Deeter et al. (2012) find that a smoothing error, which depends on the
344 retrieval averaging kernels and CO variability in the lower troposphere, exhibits strong
345 geographical and seasonal variability. Amnuaylojaroen et al. (2014) find that simulated CO
346 concentrations are significantly and consistently higher than that of MOPITT V6 data over
347 areas of biomass burning in Southeast Asia, similar to our results.

348 The primary advantage of the TES/MLS joint CO product is that it gives information on
349 vertical distributions (Fig. 13). The simulation captures the tropospheric vertical profiles
350 reasonably well (within $\pm 1\sigma$ of TES/MLS mean) at the selected locations in the northern and
351 southern hemispheres and in all seasons, except over West Africa in boreal winter during the
352 peak of biomass burning. The adjustment of the simulated CO with the TES/MLS averaging
353 kernel (AK) significantly improves the agreement above 300 mb, over all locations and in all
354 seasons while near the surface the effect is geographically varying, in agreement with other
355 studies (e.g., Deeter et al., 2012). Over the eastern US, the adjustment of simulated CO
356 causes a slightly larger positive bias compared to that without adjustment. Though simulated
357 CO is significantly improved near the surface, it is still biased high over West Africa by
358 $\sim 50\%$ during the peak of biomass burning, also consistent with other studies
359 (Amnuaylojaroen et al., 2014).

360 **4 ECCOH as a Tool for Studying the Nonlinear CH₄-CO-OH System**

361 In this section, we 1) present the justification for simulating the nonlinear chemistry of the
362 CH₄-CO-OH system as opposed to using a static climatology of OH distributions, and 2)
363 demonstrate the utility of the ECCOH chemistry module for studying the CH₄-CO-OH
364 system. In Sect. 4.1, we discuss the nontrivial, large-scale interannual variations of methane,
365 CO, and OH in our scenarios. In Sect. 4.2, we discuss the considerable spatial and temporal
366 heterogeneity of OH and methane and CO loss rates, which would not be captured if a static
367 climatology of OH distributions was used. In Sect. 4.3, we present the results of our
368 sensitivity scenarios (Table 2), which demonstrate the utility of the ECCOH chemistry
369 module for studying the CH₄-CO-OH system.

370 **4.1 Large Scale Interannual Variations in Methane, CO, and OH**

371 Even on a global scale, there are large interannual variations in methane, CO, and OH.
372 The deviations of mass-weighted concentrations of methane, CO, and OH for both the *Base*
373 and *AllVary* scenarios are shown in Fig. 14. The magnitudes of the year-to-year deviations in
374 methane are not substantially different between the two scenarios, since the *Base* scenario
375 includes the important source of variation associated with anthropogenic methane emissions
376 and methane's background is large. On the other hand, the deviations for CO and OH are far
377 greater in the *AllVary* scenario. The magnitude of the CO deviations is a factor of ten greater
378 in the *AllVary* scenario than the *Base* scenario, which has annually-repeating CO emissions.
379 The magnitude of the OH deviations increase $\pm 2\%$ to $\pm 5\%$, though as discussed below, there

380 are much larger variations on regional scales that are masked in the global average. In
381 general, CO and OH deviations are coincident, but of opposite sign as reaction of CO with
382 OH is the primary sink for both gases on a global scale. Similar deviations are seen in the
383 mid-latitudes of both hemispheres, indicating the global extent of some specific events, such
384 as large biomass burning events. These results are also consistent with Voulgarakis et al.
385 (2015) who, using full chemistry simulations, found large deviations ($> 15\%$) in CO using
386 annually-varying CO biomass burning emissions as compared to annually-repeating
387 emissions.

388 The nonlinear effects of the CH₄-CO-OH system on the temporal evolution of global
389 mass-weighted methane are smaller, but significant, as compared to the effects of variations
390 of methane emissions. The *E_{CH₄Vary}* scenario includes variations in anthropogenic and
391 natural methane emissions and also variations in meteorology (e.g., temperature, water
392 vapor) that influence the distributions of methane, CO, and OH. The *AllVary* scenario
393 includes also variations in CO emissions and all the other factors that influence OH, such as
394 the overhead ozone column, NO_x, tropospheric ozone, and VOCs. The influence of the
395 nonlinear effects of the CH₄-CO-OH system is shown in the difference of the *AllVary* and
396 *E_{CH₄Vary}* scenarios. For example, the shaded area between the two scenarios in Fig. 4
397 illustrates the combined effect of nonlinearities of the CH₄-CO-OH system on methane's
398 growth rate. The growth rate in the *AllVary* scenario is about 4 ppb/yr higher than in the
399 *E_{CH₄Vary}* scenario during the early 1990s, a time when stratospheric ozone was impacted by
400 the eruption of Mt. Pinatubo, emissions from the Soviet Union changed as it contracted
401 economically, and there was a prolonged El Niño. While these factors caused changes in
402 methane emissions, they also caused substantial variations in CO and OH (Duncan and
403 Logan, 2008) that influenced methane's growth rate. Briefly in the mid-1990s, the growth
404 rate in the *AllVary* scenario becomes lower than in the *E_{CH₄Vary}* scenario. The decline in
405 methane growth rate in 1994-1997 is primarily related to the variability of the factors that
406 influence OH (Fig. S 4) while the other non-linear feedbacks are primarily related to
407 variability in CO emissions (Fig. S 5). Worldwide, there were record wildfires in 1997 and
408 1998 that were associated with a record El Niño, which began in 1997, that transitioned to a
409 record La Niña in 1998 (Duncan et al., 2003a, 2003b). Consequently, there were large
410 variations in CO (Duncan and Logan, 2008) that causes methane's growth rate to become
411 higher again in the *AllVary* scenario. During the 2000s, a relatively quiet period with few
412 large wildfires or notable ENSO events, the growth rate is lower in the *AllVary* than the
413 *E_{CH₄Vary}* scenario. In summary, the nonlinear effects of the CH₄-CO-OH system cause
414 important fluctuations in methane's growth rate over our study period of ± 4 ppb/yr.

415 We compare simulated, mass-weighted pseudo first order rate constants (k'), a proxy for
416 OH interannual variations, from each of our scenarios to that inferred from MCF
417 measurements (Fig. 15; 1998-2007; Montzka et al., 2011). We find that none of our model
418 scenarios are able to reproduce the inferred interannual OH variability of Montzka et al.
419 (2011), though the simulated variability is of similar magnitude and within observational
420 uncertainty. Our findings are consistent with other modeling studies (Montzka et al., 2011;
421 Holmes et al., 2013; Murray et al., 2013 and references therein). While global interannual
422 variations are informative, there can be considerable OH interannual variations regionally (as
423 discussed in Sections 4.2 and 4.3) that may not be reflected in the global average (Lelieveld

424 et al., 2002; Wild and Palmer, 2008).

425 Despite the lack of agreement between the inferred and simulated OH variations, this
426 comparison exercise allows us to understand the contribution of various factors to the
427 simulated interannual variations of tropospheric OH and, subsequently, the growth rate of
428 methane (Fig. 4). As shown in Fig. 15, the *Base* scenario has $\pm 3\%$ interannual variability.
429 This scenario includes interannual variations in meteorology, such as in clouds, water vapor,
430 temperature and solar radiation, which are known to be important drivers of OH (e.g., Rohrer
431 and Berresheim, 2006; Rohrer et al., 2014). The only large deviation in OH from the *Base*
432 scenario occurs in 1997 and 1998 in the *BBE_{CO}Vary* scenario. There were several major
433 wildfires that account for this deviation, including fires in Indonesia, Mexico, and the boreal
434 forests of Asia and North America (e.g., Duncan et al., 2003a). OH is lower in the *AllVary*
435 scenario than the *Base* scenario because of higher CO emissions from the fires. For instance,
436 Duncan et al. (2003b) used a model to show that the Indonesian wildfires in 1997 depressed
437 OH levels by more than 20% over the Indian Ocean and 5-10% over much of the tropics for
438 several months. Lower OH during 1997 and 1998 in the *AllVary* scenario is consistent with
439 the higher methane growth rate as compared to the *Base* scenario (Fig. 3).

440 ENSO affects the variability of sea surface temperatures, water vapor, deep convection,
441 etc., and, subsequently, OH over large regions of the tropics. As shown in Fig. 16, the
442 deviations of mass-weighted OH from various scenarios over Indonesia (100°-150°E; 6°N-
443 6°S) are generally anti-correlated with the Multivariate ENSO Index (MEI, Wolter et al.,
444 2011), a proxy of ENSO. OH variations in the *Base* scenario, which includes meteorological
445 variations that affect OH via variations in water vapor, clouds, etc., are $\pm 4\%$ ($R^2 = 0.20$), but
446 much higher in the scenarios that include variations in biomass burning emissions (e.g.,
447 *AllVary* scenario), which better capture the ENSO variability ($R^2 = 0.59$).

448 **4.2 Spatial and Temporal Distributions of the Production/Loss Rates of** 449 **Methane and CO**

450 Any model simulation using annually-repeating and archived OH will not accurately
451 capture regional and interannual variations in the loss rates of methane and CO. A
452 simulation using zonally-averaged archived OH (e.g., Spivakovsky et al., 2000), such as was
453 done in the TransCom MIP, will not capture any regional and interannual variations. For
454 example, Fig. S 7 and Fig. S 12 reproduce Fig. 4a and Fig. 5, respectively, but include
455 methane from a simulation using archived and annually-repeating OH of the NASA Global
456 Modeling Initiative (GMI) model (Duncan et al., 2007b; Strahan et al., 2007). The simulated
457 longer methane lifetime (Fig. S 7), using archived OH, leads to an accumulation of methane
458 over the multi-decadal simulation. In this situation, the archived OH would need to be
459 adjusted higher to improve the simulation of methane as compared to observations.

460 Even though methane is relatively well mixed in the troposphere due to its long lifetime,
461 there is important spatial heterogeneity in methane's and CO's loss rates (Fig. 17 to Fig.
462 21), which is associated with the distribution of sources and reaction with OH, and changes
463 in the density of air with altitude. The global methane loss rate maximizes during boreal
464 summer and reaches a minimum during boreal winter (Fig. 17). Most methane loss occurs
465 between 30°S and 30°N (Fig. 17) since OH is most abundant in this region and methane's

466 reaction with OH is temperature dependent (Sander et al., 2011). In addition, most loss
467 occurs near the surface despite higher OH in the mid-troposphere (Fig. 2) because of higher
468 methane mole fractions near the surface (e.g., ~3 % over Alaska, but higher over source
469 regions), the altitude dependence of air density, and the temperature dependence of the loss
470 rate (Fig. 18). Methane's loss rates in the *AllVary* scenario are relatively higher, especially
471 over biomass burning regions (Fig. 17) and have much higher spatial variability than in the
472 *Base* scenario (Fig. 19). In contrast to methane, a higher proportion of CO is lost at
473 northern hemisphere mid-latitudes as the CO loss rate is less temperature dependent than
474 methane's and the lifetime is shorter (Fig. 20). The CO loss rate also varies strongly with
475 altitude (not shown), similar to that of methane. The simulated seasonal mean loss rate of
476 CO from the *AllVary* scenario is also relatively higher over biomass burning regions but
477 lower over Asia (Fig. 20), and has much higher variability that reaches up to ~20%
478 compared to about 5% in the *Base* scenario (Fig. 21).

479 **4.3 Factors that Influence the Nonlinear CH₄-CO-OH System**

480 The differences in global abundances of CO and OH between our least complex (*Base*,
481 Table 1) and most complex (*AllVary*, Table 2) scenarios are substantial and their impact on
482 methane's evolution is nontrivial as discussed in Sect. 4.1 and 4.2. Therefore, model studies
483 of methane and/or CO, which use archived fields of OH distributions, will not capture these
484 important nonlinear feedbacks of the CH₄-CO-OH system (e.g., Fig. 4). Here, we discuss the
485 contribution of various factors to the observed spatial distributions and temporal evolution of
486 observed methane, CO, and OH to demonstrate the utility of the ECCOH chemistry module
487 for studying the CH₄-CO-OH system. We provide a brief summary of our conclusions from
488 the scenarios at the end of this section.

489 *E_{CH₄}Vary Scenario*: In the *E_{CH₄}Vary* scenario, all methane emissions are annually-varying
490 (Fig. S 1). Variations in emissions from wetlands are the largest single contributor to global
491 interannual variations, with biomass burning being a lesser contributor (e.g., Bousquet et al.,
492 2006). Patra et al. (2011) reported that up to 60% of methane's observed interannual
493 variation can be explained by variations in meteorology as well as interannual variations in
494 wetland and biomass burning emissions. Given the high methane background concentration,
495 the spatial differences of methane columns between the *E_{CH₄}Vary* and *Base* scenarios are
496 rather small (about ±5 ppb (-1 to 1%)) over most of the globe when taken as seasonal
497 averages of 1988-2007 (Fig. S 19). Consistent with the annually-varying natural emissions
498 of methane, the largest differences occur over rice-producing regions of India and
499 Bangladesh (up to ~5%) and the wetlands of South America (down to -5%), including the
500 Pantanal. The simulated methane monthly variations from the *E_{CH₄}Vary* scenario are in better
501 agreement for the northern hemisphere high latitude GMD station observations as compared
502 to the *Base* scenario (Fig. S 8), which is also consistent with the findings of the TransCom
503 MIP (Patra et al., 2011). The impact of annually-varying natural methane emissions has a
504 small effect (-1% to 1%), as expected, on the spatial distributions of CO and OH because of
505 the slow reaction rate of methane with OH (Fig. S 19; Table 4).

506 *BBE_{CO}Vary* and *FFBBE_{CO}Vary Scenarios*: We developed these scenarios to understand the
507 influence of annually-varying CO emissions from biomass burning and fossil fuel

508 combustion (Fig. S 2) on the observed interannual variation of methane, CO and OH.
509 Including annually-varying biomass burning emissions (*BBE_{CO}Vary*) improves the mean
510 agreement of the simulated CO with GMD observations (mean S=0.83, $R^2 = 0.70$, Table 4),
511 but not at all individual GMD stations (Table 4). Improvements occur particularly during
512 years with large fires (e.g., 1997, 1998, 2003, 2004; Fig. 9 to Fig. 11). Adding annually-
513 varying anthropogenic CO emissions in addition to annually-varying biomass burning
514 emissions (*FFBBE_{CO}Vary*) further improves the mean comparison (mean S=0.88),
515 particularly in the northern hemisphere during the 1990s (Fig. 10). Overall, annually-varying
516 CO emissions (*FFBBE_{CO}Vary*) have a significant impact on the spatial distributions of
517 tropospheric CO ($\pm 20\%$) and OH ($\pm 10\%$) relative to the *Base* scenario, and influence
518 methane by $\pm 1\%$ (Fig. S 21, Table 4). Simulating annually-varying CO biomass burning
519 emissions (i.e., *BBE_{CO}Vary* scenario) improves simulated methane relative to the *Base*
520 scenario as compared to observations (mean S=0.97, $R^2 = 0.76$, Table 4).

521 *OH_{input}Vary* Scenario: In this scenario, we look at the impact of other causal factors that
522 influence OH, including trends in NO_x and VOC emissions and the overhead ozone column
523 (Table 2). For example, both variations in the overhead ozone column and NO emissions
524 from lightning are known to cause variations in global OH (e.g., Duncan and Logan, 2008;
525 Murray et al., 2013). Together, these causal factors have a significant influence on the spatial
526 distributions of OH ($\pm 20\%$) and CO ($\pm 5\%$) relative to the *Base* scenario and a $\pm 1\%$ effect on
527 methane (Fig. S 4, Fig. S 20, Table 4).

528 *AllVary* Scenario: In this scenario, we investigate the combined effect of all variables (Table
529 2) on the simulated distributions of methane, CO, and OH. The seasonal mean spatial (not
530 shown) and zonal (Fig. 2) distributions of OH are quite comparable to that of the *Base*
531 scenario. The interannual variations in the seasonal mean OH (Fig. 22) are significantly
532 higher ($\sim 20\%$) as compared to the *Base* scenario ($< 5\%$, sec. 3.1), which is related to the
533 annually-varying methane and CO emissions as well as OH constraints in this scenario.
534 There are large differences in the spatial distributions of methane ($\pm 5\%$), CO ($\pm 20\%$), and
535 OH ($\pm 20\%$) between the *Base* and *AllVary* scenarios (Fig. S 22, Table 4). Despite large
536 spatial differences in OH, the global, mean MCF lifetime for the *AllVary* scenario, which
537 ranges from 6.01 (± 0.51) to 6.67 (± 0.61) years over the simulation period, is not significantly
538 different from that of the *Base* scenario.

539 *Summary of Key Findings of Sensitivity Studies:* Overall, variations in anthropogenic and
540 natural methane emissions drive the majority of global variations in observed methane and
541 variations in anthropogenic and natural CO emissions drive the majority of global variations
542 in observed CO. These results are consistent with the findings of other literature studies
543 (e.g., Duncan and Logan, 2008; Patra et al., 2011). We find that the influence of variations of
544 CO emissions and factors that influence OH (e.g., overhead ozone column, VOCs, NO_x)
545 have a significant net effect on the distributions and temporal evolution of methane, CO and
546 OH. This result is consistent with the findings of Duncan and Logan (2008) for CO and OH.
547 The significant influence of the combined nonlinear feedbacks on methane is shown in the
548 difference of the *AllVary* and *E_{CH4}Vary* scenarios (e.g., Fig. 4).

549 Accurate quantification of the magnitude of the combined nonlinear feedbacks is
550 ultimately dependent on the uncertainties and errors of emissions, such as those discussed in
551 Sect. 3, and independent variables, each of which have their own uncertainties, used in the

552 parameterization of OH. With our sensitivity simulations, we discussed instances when
553 changes to emissions and/or the input to the parameterization of OH improved or worsened
554 the simulated methane and CO. In some instances, simulated methane and/or CO from the
555 least complex *Base* scenario more favorably agreed with observations than the other more
556 complex scenarios, including methane in the most complex *AllVary* scenario (e.g., Table 4,
557 Fig. 4). However, in these instances, better correlation does not necessarily imply that a
558 simpler scenario, such as the *Base* scenario or a scenario that uses archived and annually-
559 repeating OH, is inherently better. The best scenario is one that accurately simulates the
560 complex interactions of the factors that influence the CH₄-CO-OH system, which will give
561 confidence in the response of the system to perturbations, such as from large interannual
562 variations in wetland fluxes, biomass burning, ENSO, and volcanic eruptions. The next steps
563 for our research include quantifying the 1) sensitivity of the simulated CH₄-CO-OH system
564 to uncertainties in the factors (e.g., water vapor, clouds, trace gases) that control tropospheric
565 OH so as to improve simulated methane and CO with observations, and 2) the influence of
566 potential large atmospheric carbon perturbations in a warming world, such as may occur
567 from permafrost thaw, methane hydrate release, and enhanced biomass burning.

568 **5 Summary**

569 We present the fully interactive, computationally Efficient CH₄-CO-OH (ECCOH)
570 chemistry module, which we implemented in the NASA GEOS-5 AGCM. To demonstrate
571 the utility of the ECCOH chemistry module, we exercised the module with a set of scenarios
572 to simulate the influence of various causal factors on OH and the observed variations in
573 methane and CO over 1988-2007, which gives confidence in the fidelity of the module for
574 scientific research. Discrepancies between the output and observations are largely explained
575 by known deficiencies (as reported in the literature) in the methane and CO emissions used
576 as input to the ECCOH chemistry module and AGCM. Through our simulations, we show
577 the importance of using an interactive CH₄-CO-OH system as opposed to using static,
578 archived OH fields, as nonlinear feedbacks on methane, CO, and OH are non-trivial. For
579 example, nonlinear feedbacks modulate the global methane growth rate over our study
580 period (± 20 ppbv yr⁻¹) by ± 4 ppbv yr⁻¹ (Fig. 4).”

581

582

583 **Code availability**

584 The GEOS-5 source code is available under the NASA Open-Source Agreement at
585 <http://opensource.gsfc.nasa.gov/projects/GEOS-5/>.

586

587 *Acknowledgements:* This work was supported by the NASA Modeling, Analysis and
588 Prediction and Interdisciplinary Science programs. We would like to thank the
589 SCIAMACHY WFM-DOAS team at the University of Bremen IUP/IFE for using their
590 methane L3 product as well as the TES/MLS Aura team for using their L2 CO product and
591 Stephen Montzka (NOAA) for providing MCF-inferred OH deviations for comparison.
592 MOPITT CO column data were obtained from the NASA Langley Research Center
593 Atmospheric Science Data Center. We would like also to thank Stacey Frith for providing

594 the output of the GEOS-5 CCM full chemistry simulations. Earlier model development of the
595 ECCOH chemistry module by Elena Yegorova is appreciated. Useful discussions with
596 Prabir Patra (RIGC/JAMSTEC), Huisheng Bian, Junhua Liu and Jerald Ziemke (NASA
597 GSFC), as well as, technical support from Michael Manyin, Yasuko Yoshida and Eric
598 Nielsen (NASA GSFC) are gratefully acknowledged.

599 **6 References**

- 600 Amnuaylojaroen, T., Barth, M. C., Emmons, L. K., Carmichael, G. R., Kreasuwun, J.,
601 Prasitwattanaseree, S., and Chantara, S.: Effect of different emission inventories on
602 modeled ozone and carbon monoxide in Southeast Asia, *Atmos. Chem. Phys.*, 14, 12983-
603 13012, doi:10.5194/acp-14-12983-2014, 2014.
- 604 Bousquet, P., Ciais, P., Miller, J. B., Dlugokencky, E. J., Hauglustaine, D. A., Prigent, C.,
605 Van der Werf, G. R., Peylin, P., Brunke, E. G., Carouge, C., Langenfelds, R. L., Lathiere,
606 J., Papa, F., Ramonet, M., Schmidt, M., Steele, L. P., Tyler, S. C., and White, J.:
607 Contribution of anthropogenic and natural sources to atmospheric methane variability,
608 *Nature*, 443, 439–443, 2006.
- 609 Chameides, W., Liu, S. C. and Cicerone, R. J.: Possible variations in atmospheric methane, *J.*
610 *Geophys. Res.*, 81, 4997-5001, 1976.
- 611 Deeter, M. N.: MOPITT (Measurement of Pollution in the Troposphere) Version6 Product
612 User's Guide, available at:
613 http://www2.acd.ucar.edu/sites/default/files/mopitt/v6_users_guide_201309.pdf (last
614 access: May 28th 2015), 2013.
- 615 Deeter, M. N., Worden, H. M., Edwards, D. P., Gille, J. C., and Andrews, A. E.: Evaluation
616 of MOPITT retrievals of lower tropospheric carbon monoxide over the United States, *J.*
617 *Geophys. Res.*, 117, D13306, doi:10.1029/2012JD017553, 2012.
- 618 Dlugokencky, E.J., Lang, P.M., and Masarie, K.A., Atmospheric Methane Dry Air Mole
619 Fractions from the NOAA ESRL Carbon Cycle Cooperative Global Air Sampling
620 Network, 1983-2009, Version: 2010-08-12, Path: [ftp://ftp.cmdl.noaa.gov/ccg/ch4/flask/-
621 event/](ftp://ftp.cmdl.noaa.gov/ccg/ch4/flask/-event/), 2010.
- 622 Dlugokencky, E.J., Lang, P.M., Crotwell, A.M., Masarie, K.A., and Crotwell, M.J.:
623 Atmospheric Methane Dry Air Mole Fractions from the NOAA ESRL Carbon Cycle.
624 Cooperative Global Air Sampling Network, 1983-2013, Version: 2014-06-24, 2014.
- 625 Duncan, B. N., Portman, D., Bey, I., and Spivakovsky, C. M.: Parameterization of OH for
626 efficient computation in chemical tracer models, *J. Geophys. Res.*, 105 (D10), 12259–
627 12262, 2000.
- 628 Duncan, B. N., Martin, R. V., Staudt, A. C., Yevich, R. M., and Logan, J. A.: Interannual and
629 Seasonal Variability of Biomass Burning Emissions Constrained by Satellite Observations,
630 *J. Geophys. Res.*, 108(D2), 4040, doi:10.1029/2002JD002378, 2003a.
- 631 Duncan, B.N., I. Bey, M. Chin, L.J. Mickley, T.D. Fairlie, R.V. Martin, and H. Matsueda,
632 Indonesian Wildfires of 1997: Impact on Tropospheric Chemistry, *J. Geophys. Res.*, 108,
633 D15, 4458, doi:10.1029/2002JD003195, 2003b.
- 634 Duncan, B. N., Logan, J. A., Bey, I., Megretskaya, I. A., Yantosca, R. M., Novelli, P. C.,
635 Jones, N. B., and Rinsland, C. P.: Global budget of CO, 1988–1997: Source estimates and

636 validation with a global model, *J. Geophys. Res.*, 112(D22), D22301,
637 doi:10.1029/2007JD008459, 2007a.

638 Duncan, B. N., Strahan, S. E., Yoshida, Y., Steenrod, S. D., and Livesey, N.: Model study of
639 the cross-tropopause transport of biomass burning pollution, *Atmos. Chem. Phys.*, 7,
640 3713–3736, doi:10.5194/acp-7-3713-2007, 2007b.

641 Duncan, B. and Logan, J.: Model analysis of the factors regulating the trends and variability
642 of carbon monoxide between 1988 and 1997, *Atmos. Chem. Phys.*, 8, 7389-7403, 2008.

643 Elshorbany, Y. F, Barnes, I., Becker, K. H, Kleffmann, J., and Wiesen, P.: Sources and
644 Cycling of Tropospheric Hydroxyl Radicals-An Overview, *Zeitschrift für Physikalische*
645 *Chemie*, 224, 967-987, DOI:10.1524/zpch.2010.6136, 2010.

646 Elshorbany, Y. F., Kleffmann, J., Hofzumahaus, A., Kurtenbach, R., Wiesen, P., Dorn, H.-P.,
647 Schlosser, E., Brauers, T., Fuchs, H., Rohrer, F., Wahner, A., Kanaya, Y., Yoshino, A.,
648 Nishida, S., Kajii, Y., Martinez, M., Rudolf, M., Harder, H., Lelieveld, J., Elste, T., Plass-
649 Dülmer, C., Stange, G., and Berresheim, H.: HO_x Budgets during HO_xComp: a Case
650 Study of HO_x Chemistry under NO_x limited Conditions, *J. Geophys. Res.*, 117, D03307,
651 doi: 10.1029/2011JD017008, 2012a.

652 Elshorbany, Y. F., Steil, B., Brühl, C., and Lelieveld, J.: Impact of HONO on global
653 atmospheric chemistry calculated with an empirical parameterization in the EMAC model,
654 *Atmos. Chem. Phys.*, 12, 9977-10000, doi:10.5194/acp-12-9977-2012, 2012b.

655 Elshorbany, Y. F., Crutzen, P. J., Steil, B., Pozzer, A., Tost, H., and Lelieveld, J.: Global and
656 regional impacts of HONO on the chemical composition of clouds and aerosols, *Atmos.*
657 *Chem. Phys.*, 14, 1167-1184, doi:10.5194/acp-14-1167-2014, 2014.

658 Fiore, A. M., Jacob, D. J., Field, B. D., Streets, D. G., Fernandes, S. D., and Jang, C. :
659 Linking air pollution and climate change: The case for controlling methane, *Geophys. Res.*
660 *Lett.*, 29(19), 1919, doi:10.1029/2002GL015601, 2002.

661 Fiore, A. M., Horowitz, L. W., Dlugokencky, E. J. and West, J. J.: Impact of meteorology
662 and emissions on methane trends, 1990-2004, *Geophys. Res. Lett.*, 33, L12809,
663 doi:10.1029/2006GL026199, 2006.

664 Fiore, A.M., Dentener, F.J., Wild, O., Cuvelier, C., Schultz, M.G., Hess, P., Textor, C.,
665 Schulz, M., Doherty, R.M., Horowitz, L.W., MacKenzie, I.A., Sanderson, M.G., Shindell,
666 D.T., Stevenson, D.S., Szopa, S., Van Dingenen, R., Zeng, G., Atherton, C., Bergmann,
667 D., Bey, I., Carmichael, G., Collins, W.J., Duncan, B.N., Faluvegi, G., Folberth, G.,
668 Gauss, M., Gong, S., Hauglustaine, D., Holloway, T., Isaksen, I.S.A., Jacob, D.J., Jonson,
669 J.E., Kaminski, J.W., Keating, T.J., Lupu, A., Marnmer, E., Montanaro, V., Park, R.J.,
670 Pitari, G., Pringle, K.J., Pyle, J.A., Schroeder, S., Vivanco, M.G., Wind, P., Wojcik, G.,
671 Wu, S., Zuber, A.: Multimodel estimates of intercontinental source-receptor relationships
672 for ozone pollution, *J. Geophys. Res.*, 114, D04301, doi:10.1029/2008JD010816, 2009.

673 Fujino J, Nair R, Kainuma M, Masui T, Matsuoka Y, Multigas mitigation analysis on
674 stabilization scenarios using aim global model. *The Energy Journal Special issue #3*:343–
675 354, 2006.

676 Frankenberg, C., Aben, I., Bergamaschi, P., Dlugokencky, E. J., van Hees, R., Houweling,
677 S., van der Meer, P., Snel, R., Tol, P.: Global column-averaged methane mixing ratios from
678 2003 to 2009 as derived from SCIAMACHY: Trends and variability, *J. of Geophys. Res.*,
679 116, D04302, doi: 10.1029/2010JD014849, 2011.

680 Fuchs, H., Hofzumahaus, A., Rohrer, F., Bohn, B., Brauers, T., Dorn, H.-P., Haßeler, R.,
681 Holland, F., Kaminski, M., Li, X., Lu, K., Nehr, S., Tillmann, R., Wegener, R., Wahner,
682 A.: Experimental evidence for efficient hydroxyl radical regeneration in isoprene
683 oxidation. *Nat. Geosci.* 6, 1023-1026, doi:10.1038/ngeo1964, 2013.

684 Giglio, L., Randerson, J. T., van der Werf, G. R., Kasibhatla, P. S., Collatz, G. J., Morton, D.
685 C., and DeFries, R. S.: Assess- ing variability and long-term trends in burned area by
686 merging multiple satellite fire products, *Biogeosciences*, 7, 1171–1186, doi:10.5194/bg-7-
687 1171-2010, 2010.

688 Gloudemans, A. M. S., Schrijver, H., Hasekamp, O. P., and Aben, I.: Error analysis for CO
689 and CH₄ total column retrievals from SCIAMACHY 2.3 μm spectra, *Atmos. Chem. Phys.*,
690 8, 3999-4017, doi:10.5194/acp-8-3999-2008, 2008.

691 Hijioka Y, Matsuoka Y, Nishimoto H, Masui T, Kainuma M.: Global GHG emission
692 scenarios under GHG concentration stabilization targets. *J Glob Environ Eng* 13:97–108,
693 2008.

694 Ho, S.-P., Edwards, D. P., Gille, J. C., Luo, M., Osterman, G. B., Kulawik, S. S., and
695 Worden, H.: A global comparison of carbon monoxide profiles and column amounts from
696 Tropospheric Emission Spectrometer (TES) and Measurements of Pollution in the
697 Troposphere (MOPITT), *J. Geophys. Res.*, 114, D21307, doi:10.1029/2009JD012242,
698 2009.

699 Holmes, C. D., Prather, M. J., Søvde, O. A., and Myhre, G.: Future methane, hydroxyl, and
700 their uncertainties: key climate and emission parameters for future predictions, *Atmos.*
701 *Chem. Phys.*, 13, 285-302, doi:10.5194/acp-13-285-2013, 2013.

702 Houweling, S., Krol, M., Bergamaschi, P., Frankenberg, C., Dlugokencky, E. J., Morino, I.,
703 Notholt, J., Sherlock, V., Wunch, D., Beck, V., Gerbig, C., Chen, H., Kort, E. A.,
704 Röckmann, T., and Aben, I.: A multi-year methane inversion using SCIAMACHY,
705 accounting for systematic errors using TCCON measurements, *Atmos. Chem. Phys.*, 14,
706 3991-4012, doi:10.5194/acp-14-3991-2014, 2014.

707 Lamarque, J.-F., Shindell, D. T., Josse, B., Young, P. J., Cionni, I., Eyring, V., Bergmann,
708 D., Cameron-Smith, P., Collins, W. J., Doherty, R., Dalsoren, S., Faluvegi, G., Folberth,
709 G., Ghan, S. J., Horowitz, L. W., Lee, Y. H., MacKenzie, I. A., Nagashima, T., Naik, V.,
710 Plummer, D., Righi, M., Rumbold, S. T., Schulz, M., Skeie, R. B., Stevenson, D. S.,
711 Strode, S., Sudo, K., Szopa, S., Voulgarakis, A., and Zeng, G.: The Atmospheric
712 Chemistry and Climate Model Intercomparison Project (ACCMIP): overview and
713 description of models, simulations and climate diagnostics, *Geosci. Model Dev.*, 6, 179–
714 206, doi:10.5194/gmd-6-179-2013, 2013.

715 Lawrence, M. G., Jöckel, P., and von Kuhlmann, R.: What does the global mean OH
716 concentration tell us?, *Atmos. Chem. Phys.*, 1, 37-49, doi:10.5194/acp-1-37-2001, 2001.

717 Lelieveld, J., Peters, W., Dentener, F. J., and Krol, M. C.: Stability of tropospheric hydroxyl
718 chemistry, *J. Geophys. Res.*, 107(D23), 4715, doi:10.1029/2002JD002272, 2002.

719 Lin, S.-J.: A “vertically Lagrangian” finite-volume dynamical core for global models, *Mon.*
720 *Weather Rev.*, 132(10), 2293–2307, 2004.

721 Luo, M., Read, W., Kulawik, S., Worden, J., Livesey, N., Bowman, K. and Herman, R.:
722 Carbon monoxide (CO) vertical profiles derived from joined TES and MLS measurements,
723 *J. Geophys. Res. Atmos.*, 118, 10601–10613, doi:10.1002/jgrd.50800, 2013.

724 Molod, A., Takacs, L., Suarez, M., Bacmeister, J., Song, I.-S., and Eichmann, A.: The
725 GEOS-5 Atmospheric General Circulation Model: Mean Climate and Development from
726 MERRA to Fortuna, NASA/TM-2012-104606, Technical Report Series on Global
727 Modeling and Data Assimilation, Vol. 28, edited by: Suarez, M., available at:
728 <http://gmao.gsfc.nasa.gov/pubs/docs/tm28.pdf> (last access: October 27, 2015), 2012.

729 Monks, S. A., Arnold, S. R., Emmons, L. K., Law, K. S., Turquety, S., Duncan, B. N.,
730 Flemming, J., Huijnen, V., Tilmes, S., Langner, J., Mao, J., Long, Y., Thomas, J. L.,
731 Steenrod, S. D., Raut, J. C., Wilson, C., Chipperfield, M. P., Diskin, G. S.,
732 Weinheimer, A., Schlager, H., and Ancellet, G.: Multi-model study of chemical and
733 physical controls on transport of anthropogenic and biomass burning pollution to the
734 Arctic, *Atmos. Chem. Phys.*, 15, 3575-3603, doi:10.5194/acp-15-3575-2015, 2015.

735 Montzka, S. A., Krol, M., Dlugokencky, E., Hall, B., Joeckel, P., and Lelieveld, J.: Small
736 interannual variability of global atmospheric hydroxyl, *Science*, 331, 67-69,
737 doi:10.1126/science.1197640, 2011.

738 Murray, L. T., Logan, J. A., and Jacob, D., J.: Interannual variability in tropical tropospheric
739 ozone and OH: The role of lightning, *J. Geophys. Res. Atmos.*, 118, 11,468-11,480,
740 doi:10.1002/jgrd.50857, 2013.

741 Myhre, G., Shindell, D., Breion, F.-M., Collins, W., Fuglestedt, J., Huang, J., Koch, D.,
742 Lamarque, J.-F., Lee, D., 5 Mendoza, B., Nakajima, T., Robock, A., Stephens, G.,
743 Takemura, T., and Zhang, H.: Anthropogenic and natural radiative forcing, in: *Climate
744 Change 2013: The Physical Science Basis. Contribution of Working Group I to the Fifth
745 Assessment Report of the Intergovernmental Panel on Climate Change*, edited by: Stocker,
746 T. F., Qin, D., Plattner, G.-K., Tignor, M., Allen, S. K., Boschung, J., Nauels, A., Xia, Y.,
747 Bex, V., and Midgley, P. M., available at:
748 http://www.climatechange2013.org/images/report/WG1AR5_ALL_FINAL.pdf (last
749 access: October 27, 2015), 2013.

750 Naik, V., Voulgarakis, A., Fiore, A. M., Horowitz, L. W., Lamarque, J.-F., Lin, M.,
751 Prather, M. J., Young, P. J., Bergmann, D., Cameron-Smith, P. J., Cionni, I.,
752 Collins, W. J., Dalsøren, S. B., Doherty, R., Eyring, V., Faluvegi, G., Folberth, G. A.,
753 Josse, B., Lee, Y. H., MacKenzie, I. A., Nagashima, T., van Noije, T. P. C.,
754 Plummer, D. A., Righi, M., Rumbold, S. T., Skeie, R., Shindell, D. T., Stevenson, D. S.,
755 Strode, S., Sudo, K., Szopa, S., and Zeng, G.: Preindustrial to present-day changes in
756 tropospheric hydroxyl radical and methane lifetime from the Atmospheric Chemistry and
757 Climate Model Intercomparison Project (ACCMIP), *Atmos. Chem. Phys.*, 13, 5277-5298,
758 doi:10.5194/acp-13-5277-2013, 2013.

759 Novelli, P., Steele, P., Tans, P. P.: Mixing ratios of carbon monoxide in the troposphere, *J.
760 Geophys. Res.*, 102, 12,855-12,861, doi: 10.1029/92JD02010, 1992.

761 Novelli, P., Masarie, K., A., Lang, P. M.: Distributions and recent changes in carbon
762 monoxide in the lower troposphere, *J. Geophys. Res.*, 103, 19,015-19,033, 1998.

763 Oman, L. D., J. R. Ziemke, A. R. Douglass, D. W. Waugh, C. Lang, J. M. Rodriguez, and J.
764 E. Nielsen (2011), The response of tropical tropospheric ozone to ENSO, *Geophys. Res.
765 Lett.*, 38, L13706, doi:10.1029/2011GL047865, 2011.

766 Ott, L., Duncan, B., Pawson, S., Colarco, P., Chin, M., Randles, C., Diehl, T., and Nielsen,
767 E.: Influence of the 2006 Indonesian biomass burning aerosols on tropical dynamics

768 studied with the GEOS5 AGCM, *J. Geophys. Res.*, 115, D14121,
769 doi:10.1029/2009JD013181, 2010.

770 Patra, P. K., Houweling, S., Krol, M., Bousquet, P., Belikov, D., Bergmann, D., Bian, H.,
771 Cameron-Smith, P., Chipperfield, M. P., Corbin, K., Fortems-Cheiney, A., Fraser, A.,
772 Gloor, E., Hess, P., Ito, A., Kawa, S. R., Law, R. M., Loh, Z., Maksyutov, S., Meng, L.,
773 Palmer, P. I., Prinn, R. G., Rigby, M., Saito, R., and Wilson, C.: TransCom model
774 simulations of CH₄ and related species: linking transport, surface flux and chemical loss
775 with CH₄ variability in the troposphere and lower stratosphere, *Atmos. Chem. Phys.*, 11,
776 12813-12837, doi:10.5194/acp-11-12813-2011, 2011.

777 Patra, P. K., Krol, M. C., Montzka, S. A., Arnold, T., Atlas, E. L., Lintner, B. R., Xiang B.,
778 Elkins J. W., Fraser P. J., Ghosh A., Hints E.J., Hurst D. F., Ishijima K., Krummel P. B.,
779 Miller B. R., Miyazaki K., Moore F. L., Mühle J., O'Doherty S., Prinn R. G., Steele L. P.,
780 Takigawa M., Wang H. J., Weiss R. F., Wofsy S. C., Young, D.: Observational evidence
781 for interhemispheric hydroxyl-radical parity. *Nature*, 513(7517), 219-23, doi:
782 10.1038/nature13721, 2014.

783 Pawson, S., R., Stolarski, S., Douglass, A. R., Newman, P. A., Nielsen, J. E., Frith, S. M.,
784 and Gupta, M. L.: Goddard Earth Observing System chemistry-climate model simulations
785 of stratospheric ozone-temperature coupling between 1950 and 2005, *J. Geophys. Res.*,
786 113, D12103, doi:10.1029/2007JD009511, 2008.

787 Prather, M., and Spivakovsky, C. M.: Tropospheric OH and the lifetimes of
788 hydrochlorofluorocarbons, *J. Geophys. Res.*, 95(D11), 18723–18729,
789 doi:[10.1029/JD095iD11p18723](https://doi.org/10.1029/JD095iD11p18723), 1990.

790 Prather, M.: Lifetimes and Eigen states in atmospheric chemistry, *Geophys. Res. Lett.*, 21, 9,
791 801-804, 1994.

792 Prather, M.: Time scales in atmospheric chemistry: Theory, GWPs for CH₄ and CO, and
793 runaway growth, *Geophys. Res. Lett.*, 23, 19, 2597–2600, DOI: 10.1029/96GL02371,
794 1996.

795 Prather, M. J., C. D. Holmes, and J. Hsu.: Reactive greenhouse gas scenarios: Systematic
796 exploration of uncertainties and the role of atmospheric chemistry, *Geophys. Res. Lett.*,
797 39, L09803, doi:10.1029/2012GL051440, 2012.

798 Prinn, R. G., Huang, J., Weiss, R. F., Cunnold, D. M., Fraser, P. J., Simmonds, P. G.,
799 McCulloch, A., Harth, C., Reimann, S., Salameh, P., O'Doherty, S., Wang, R. H. J.,
800 Porter, L. W., Miller, B. R., and Krummel, P. B.: Evidence for variability of atmospheric
801 hydroxyl radicals over the past quarter century, *Geophys. Res. Lett.*, 32, L07809,
802 doi:10.1029/2004GL022228, 2005.

803 Randerson, J.T., G.R. van der Werf, L. Giglio, G.J. Collatz, and P.S. Kasibhatla.. Global Fire
804 Emissions Database, Version 3 (GFEDv3.1). Data set. Available at: <http://daac.ornl.gov>
805 (last access: October 27, 2015) from Oak Ridge National Laboratory Distributed Active
806 Archive Center, Oak Ridge, Tennessee, USA. doi:10.3334/ORNLDAAC/1191, 2013.

807 Rienecker, M. M., Suarez, M. J., Todling, R., Bacmeister, J., Takacs, L., Liu, H.-C., Gu, W.,
808 Sienkiewicz, M., Koster, R. D., Gelaro, R., Stajner, I., and Nielsen, J. E.: The GEOS-5
809 data assimilation system – Documentation of Versions 5.0.1, 5.1.0, and 5.2.0, Technical
810 Report Series on Global Modeling and Data Assimilation, Vol. 27, available at:

811 http://gmao.gsfc.nasa.gov/pubs/docs/GEOS5_104606-Vol27.pdf (last access: October 27,
812 2015), 2008.

813 Rohrer, F., and Berresheim, H.: Strong correlations between levels of tropospheric hydroxyl
814 radicals and solar ultraviolet radiation, *Nature*, 442, 184-187, doi:10.1038/nature04924,
815 2006.

816 Rohrer, F., Lu, K., Hofzumahaus, A., Bohn, B., Brauers, T., Chang, C.-C., Fuchs, H.,
817 Häsel, R., Holland, F., Hu, M., Kita, K., Kondo, Y., Li, X., Lou, S., Oebel, A., Shao, M.,
818 Zeng, L., Zhu, T., Zhang, Y., and Wahner, A.: Maximum efficiency in the hydroxyl-
819 radical-based self-cleansing of the troposphere, *Nature Geoscience* 7, 559–563,
820 doi:10.1038/ngeo2199, 2014.

821 Sander, S. P., Abbatt, J., Barker, J. R., Burkholder, J. B., Friedl, R. R., Golden, D. M., Huie,
822 R. E., Kolb, C. E., Kurylo, M. J., Moortgat, G. K., Orkin, V. L. and Wine, P. H.: Chemical
823 Kinetics and Photochemical Data for Use in Atmospheric Studies, Evaluation No. 17, JPL
824 Publication 10-6, Jet Propulsion Laboratory, Pasadena, available at:
825 <http://jpldataeval.jpl.nasa.gov> (last access: October 27, 2015), 2011.

826 Schneising, O., Buchwitz, M., Burrows, J. P., Bovensmann, H., Bergamaschi, P., and Peters,
827 W.: Three years of greenhouse gas column-averaged dry air mole fractions retrieved from
828 satellite – Part 2: Methane, *Atmos. Chem. Phys.*, 9, 443–465, doi:10.5194/acp-9-443-
829 2009, 2009.

830 Schneising, O., Buchwitz, M., Reuter, M., Heymann, J., Bovensmann, H., and Burrows, J.
831 P.: Long-term analysis of carbon dioxide and methane column-averaged mole fractions
832 retrieved from SCIAMACHY, *Atmos. Chem. Phys.*, 11, 2863– 2880, doi:10.5194/acp-
833 11-2863-2011, 2011.

834 Schultz, M., S. Rast, M. van het Bolscher, T. Pulles, R. Brand, J. Pereira, B. Mota, A.
835 Spessa, S. Dalsøren, T. van Noije, S. Szopa, Emission data sets and methodologies for
836 estimating emissions, RETRO project report D1-6, Hamburg, 26 Feb 2007, available at:
837 http://gcmd.gsfc.nasa.gov/records/GCMD_GEIA_RETRO.html (last access: October 27,
838 2015), 2007.

839 Shindell, D. T., Faluvegi, G., Stevenson, D. S., Krol, M. C., Emmons, L. K., Lamarque, J.-F.,
840 Petron, G., Dentener, F. J., Ellingsne, K., Schultz, M. G., Wild, O., Amann, M., Atherton,
841 C. S., Bergmann, D. J., Bey, I., Butler, T., Cofala, J., Collins, W. J., Derwent, R. G.,
842 Doherty, R. M., Drevet, J., Eskes, H. J., Fiore, A. M., Gauss, M., Hauglustaine, D. A.,
843 Horowitz, L.W., Isaksen, I. S. A., Lawrence, M. G., Montanaro, V., Müller, J.-F., Pitari,
844 G., Prather, M. J., Pyle, J. A., Rast, S., Rodriguez, J. M., Sanderson, M. G., Savage, N. H.,
845 Strahan, S. E., Sudo, K., Szopa, S., Unger, N., van Noije, T. P. C., and Zeng, G.:
846 Multimodel simulations of carbon monoxide: Comparison with observations and projected
847 near-future changes, *J. Geophys. Res.*, 111, D19306, doi:10.1029/2006JD007100, 2006.

848 Spivakovsky, C., Wofsy, S., and Prather, M.: A numerical method for the parameterization of
849 atmospheric chemistry: Computation of tropospheric OH, *J. Geophys. Res.*, 95, 18,433-
850 18,439, 1990a.

851 Spivakovsky, C.M., Yevich, R., Logan, J.A., Wofsy, S.C., McElroy, M.B., and Prather, M.J.,
852 Tropospheric OH in a three-dimensional chemical tracer model: An assessment based
853 on observations of CH₃CCl₃, *J. Geophys. Res.*, 95, 18,441-18,471,
854 doi:10.1029/JD095iD11p18441, 1990b.

855 Spivakovsky, C M., Logan, J A., Montzka, S A., Balkanski, Y J. Foreman-Fowler, M.,
856 Jones, D B A., Horowitz, L W., Fusco, A C., Brenninkmeijer, C A M., Prather, M J.,
857 Wofsy, S C., and McElroy, M B.: Three-dimensional climatological distribution of
858 tropospheric OH: Update and evaluation, *J. Geophys. Res.*, 105, D7, 8931–8980,
859 doi:10.1029/1999JD901006, 2000.

860 Stone, D., L.K. Whalley, D.E. Heard.: Tropospheric OH and HO₂ radicals: field
861 measurements and model comparisons. *Chemical Society Reviews*, 41:19, 6348,
862 doi:10.1039/c2cs35140d, 2012.

863 Strahan, S.E., B.N. Duncan and P. Hoor, Observationally-derived diagnostics of transport in
864 the lowermost stratosphere and their application to the GMI chemistry transport model,
865 *Atmos. Chem. Phys.*, 7, 2435-2445, 2007.

866 Strode, S. A., Duncan, B. N., Yegorova, E. A., Kouatchou, J., Ziemke, J. R., and
867 Douglass, A. R.: Implications of model bias in carbon monoxide for methane lifetime,
868 *Atmos. Chem. Phys. Discuss.*, 15, 20305-20348, doi:10.5194/acpd-15-20305-2015, 2015.

869 Voulgarakis, A., Naik, V., Lamarque, J.-F., Shindell, D. T., Young, P. J., Prather, M. J.,
870 Wild, O., Field, R. D., Bergmann, D., Cameron-Smith, P., Cionni, I., Collins, W. J.,
871 Dalsøren, S. B., Doherty, R. M., Eyring, V., Faluvegi, G., Folberth, G. A.,
872 Horowitz, L. W., Josse, B., MacKenzie, I. A., Nagashima, T., Plummer, D. A., Righi, M.,
873 Rumbold, S. T., Stevenson, D. S., Strode, S. A., Sudo, K., Szopa, S., and Zeng, G.:
874 Analysis of present day and future OH and methane lifetime in the ACCMIP simulations,
875 *Atmos. Chem. Phys.*, 13, 2563-2587, doi:10.5194/acp-13-2563-2013, 2013.

876 Voulgarakis, A., M. E. Marlier, G. Faluvegi, D. T. Shindell, K. Tsigaridis, and S. Mangeon,
877 Interannual variability of tropospheric trace gases and aerosols: The role of biomass
878 burning emissions, *J. Geophys. Res. Atmos.*, 120, 7157–7173,
879 doi:10.1002/2014JD022926, 2015.

880 Wang, J. S., Logan, J. A., McElroy, M. B., Duncan, B. N., Megretskaja, I. A., Yantosca, R.
881 M.: A 3-D model analysis of the slowdown and interannual variability in the methane
882 growth rate from 1988 to 1997, *Global Biogeochemical Cycles*, 18, GB3011,
883 doi:10.1029/2003GB002180, 2004.

884 Wang, J. S., McElroy, M. B., Logan, J. A., Palmer, P. I., Chameides, W. L., Wang, Y., and
885 Megretskaja, I. A.: A quantitative assessment of uncertainties affecting estimates of global
886 mean OH derived from methyl chloroform observations, *J. Geophys. Res.*, 113, D12302,
887 doi:10.1029/2007JD008496, 2008.

888 Wainwright, C. D., Pierce, J. R., Liggio, J., Strawbridge, K. B., Macdonald, A. M., and
889 Leaitch, R. W.: The effect of model spatial resolution on Secondary Organic Aerosol
890 predictions: a case study at Whistler, BC, Canada, *Atmos. Chem. Phys.*, 12, 10911-10923,
891 doi:10.5194/acp-12-10911-2012, 2012.

892 Wild, O., and Palmer, P. I.: How sensitive is tropospheric oxidation to anthropogenic
893 emissions?, *Geophys. Res. Lett.*, 35, L22802, doi:10.1029/2008GL035718, 2008.

894 Wolter, K., and M. S. Timlin, El Niño/Southern Oscillation behaviour since 1871 as
895 diagnosed in an extended multivariate ENSO index (MEI.ext). *Intl. J. Climatology*, 31,
896 1074-1087, DOI: 10.1002/joc.2336, 2011.

897 Worden, H. M., Deeter, M. N., Edwards, D. P., Gille, J. C., Drummond, J. R., and Nédélec,
898 P.: Observations of near-surface carbon monoxide from space using MOPITT

899 multispectral retrievals, *J. Geophys. Res.*, 115, D18314, doi:10.1029/2010JD014242,
900 2010.
901

903 Table 1: Reference Scenario (*Base*) Description

AGCM Input	Description ^a
Dynamics	Model dynamics are constrained by sea surface temperatures and sea ice concentrations from the Community Climate System Model (http://www.cesm.ucar.edu/models/ccsm4.0/ , CCSM-4) through 2005 and from 2006 to 2007 from CCSM-4 with Representative Concentration Pathways (RCP 6.0, Fujino et al. (2006); Hijioka et al. (2008)). The methane tracer is radiatively inactive and archived annually-varying methane fields used in the radiation code; our aim is reproduce the same meteorology in all simulations so as to more cleanly isolate the impact of the causal factors on methane, CO, and OH trends and variations.
<i>Parameterization of OH Input</i>	
Chemical Variables	Nitrogen oxides (as a family), ozone, overhead ozone column, and various VOCs are monthly, archived fields for 2000 and are repeated for each year of the <i>Base</i> simulation; these fields were taken from a one year (2000) GEOS-5 AGCM simulation, which was part of the ACCMIP study (Lamarque et al., 2013), with a full-representation of ozone-NO _x -VOC photochemistry (Duncan et al., 2007b; Strahan et al., 2007) and emissions of NO _x , VOCs, and species important to the stratospheric ozone layer (e.g., N ₂ O, HFCs, CFCs).
Meteorological Variables	Pressure, temperature, cloud albedo and water vapor are taken from the AGCM as the simulation progresses.
<i>Emissions^b</i>	
Methane	Annually-repeating natural (e.g., wetlands, biomass burning) and annually-varying anthropogenic emissions (EDGAR 3.2, TransCom CTL scenario) are described in Patra et al. (2011).
CO	Annually-repeating emissions representative for year 2000 time slice of the ACCMIP (Lamarque et al., 2013; Strode et al., 2015).
<i>Methane Oxidation</i>	
Troposphere	CH ₄ + OH → αCO; tropospheric OH calculated by parameterization of OH. CO yield (α) = 1 (Duncan et al., 2007a).
Stratosphere	Calculated based on its reaction with OH, Cl and O ¹ D from archived monthly fields from one year of an AGCM simulation.
<i>VOC Oxidation^b</i>	VOC + OH → αCO; CO yield (α) varies with VOC (Duncan et al., 2007b). Isoprene + OH → αCO, where CO yield (α) varies with [NO _x] (Duncan et al., 2007a).

904 ^aAll scenarios are for 1988-2007. We use the methane initial condition of 1655 ppb by January 1988 at the GMD South Pole (SPO) station,
905 (Patra et al., 2011, TransCom protocolv7), which was reached after a 12-year model spin up; results are thus considered valid from January 1,
906 1988.

907 ^bOnly methane and CO are treated as emission fluxes. The source of CO via VOC oxidation is calculated using archived, 3d fields from a GEOS-5 AGCM full chemistry

910 Table 2: Description of Simulation Scenarios

Model Scenario	Relation to Other Scenarios	Purpose of Scenario
1. <i>Base</i>	Table 1.	Reference scenario
2. <i>E_{CH4}Vary</i> <i>Base + all methane source types varying annually</i>	Same as <i>Base</i> , except that the “EXTRA” methane emission scenario is used (Patra et al., 2011). The primary difference between the CTL and EXTRA scenarios is that the CTL emissions are composed of repeating annual cycles of all source types, except for anthropogenic emissions which varies from year-to-year, while the EXTRA emission scenario has all source types (e.g., biomass burning, wetlands, rice paddies, etc.) varying annually (Fig. S 1).	To understand the influence of interannual variations in natural sources of methane on the trends and variations of model OH and observed methane and CO distributions. Wetlands are the largest single source of methane and the largest source of interannual variations (e.g., Patra et al., 2011; Voulgarakis et al., 2015).
3. <i>BBE_{CO}Vary</i> <i>Base + BB CO emissions varying annually</i>	Same as <i>Base</i> , except CO emissions from biomass burning (BB) annually vary. Emissions are from the REanalysis of the TROpospheric chemical composition (RETRO v2.0, Schultz et al., 2007) emission inventory for 1988-1996 and the Global Fire Emissions Database (GFEDv3.1, Giglio et al., 2010; Randerson et al., 2013) for years 1997-2007.	To understand the influence of interannual variations in the biomass burning source of CO (Fig. S 2). From 1988-2007, there were several large events, such as in Indonesia in 1997 [Duncan et al., 2003a] and 2006 and worldwide in 1998 [Duncan et al., 2003b].
4. <i>FFBBE_{CO}Vary</i> <i>Base + FF and BB CO emissions varying annually</i>	Same as <i>BBE_{CO}Vary</i> , except CO emissions from fossil fuels annually vary. Anthropogenic emissions are from the Emission Database for Global Atmospheric Research (EDGARv4.2) for 1988-2007.	To understand the combined influence of interannual variations in the anthropogenic and biomass burning sources of CO.
5. <i>OH_{Input}Vary</i> <i>Base + parameterization of OH chemical variables varying annually</i>	Same as <i>Base</i> , except the monthly, archived chemical variables used as input to the parameterization of OH are annually varying. Taken from the same GEOS-5 AGCM simulation as in <i>Base</i> scenario with a full-representation of ozone-NO _x -VOC photochemistry and annually varying anthropogenic and biogenic emissions of NO _x , VOCs, and species important to the stratospheric ozone layer (e.g., N ₂ O, HFCs, CFCs) (Strahan et al., 2007; Duncan et al., 2007b; Oman et al., 2011).	To understand the influence of interannual variations in other factors that affect OH. These factors include the overhead ozone column, NO _x and anthropogenic VOCs.
6. <i>AllVary</i> <i>Base + E_{CH4}Vary + FFBBE_{CO}Vary + OH_{Input}Vary</i>	Annually varying methane and CO emissions from all sources and annually-varying factors that influence OH.	To understand the combined influence of annually-varying 1) CO emissions from fossil fuel and biomass burning, 2) effects of NO _x and VOCs on OH, and 3) methane emissions from all sources.

911

912 Table 3: Data Used In Model Evaluation of Methane, CO, and OH

Data	Species	Quantity	Time Range	Reference
NOAA ESRL Global Monitoring Division (GMD) surface data	CO, methane	mixing ratio (ppbv)	1980-present	Novelli et al., 1992, 1998; Dlugokencky et al., 2010, 2014.
Envisat SCanning Imaging Absorption spectroMeter for Atmospheric CHartography (SCIAMACHY) ^a	methane	atmospheric column (molec/cm ²)	2003-2005	Bovensmann et al., 1999; Schneising et al., 2009; Schneising et al., 2011; Frankenberg et al., 2011
Terra Measurement of Pollution In The Troposphere (MOPITT) Instrument ^b	CO	atmospheric column (molec/cm ²)	1999-present	Worden, 2010; Deeter et al., 2012; Deeter, 2013.
Aura Tropospheric Emission Spectrometer (TES)/Microwave Limb Sounder (MLS) Joint Product	CO	mixing ratio (ppbv)	8/2004-10/2012	Luo et al., 2013
NOAA surface network	MCF	OH interannual variability (IAV) ^c	1997-2007	Montzka et al., 2011

913 ^aWe use version 3.7 gridded product of the column-averaged methane dry mole fraction (Schneising et al., 2009; [http://www.iup.uni-](http://www.iup.uni-bremen.de/sciamachy/NIR_NADIR_WFM_DOAS/products)
 914 [bremen.de/sciamachy/NIR_NADIR_WFM_DOAS/products](http://www.iup.uni-bremen.de/sciamachy/NIR_NADIR_WFM_DOAS/products)). The methane data since November 2005 are considered to be of reduced quality (in comparison to data from
 915 2003-October 2005) due to detector degradation in the spectral range used for the methane column retrieval (Schneising et al., 2011; Frankenberg et al., 2011).

916 ^bWe use the gridded monthly CO retrievals (thermal infrared radiances) V006 L3 product (<http://eosweb.larc.nasa.gov>)

917 ^cThere are only very sparse and uncertain direct observations (e.g., Stone et al., 2012).

918

919 Table 4: list of the correlation parameters of the different model scenarios and the monthly
 920 GMD measurements for the simulation period (1988-2007)

Scenario	ALT ^a		BRW		NWR		MLO		RPB		SPO	
	S*	R ^{2**}	S	R ²	S	R ²	S	R ²	S	R ²	S	R ²
CH₄ data												
<i>Base</i>	0.56	0.66	0.57	0.60	0.76	0.64	0.76	0.58	0.68	0.82	0.79	0.91
<i>E_{CH4}Vary</i>	0.74	0.68	0.74	0.56	0.74	0.63	0.79	0.57	0.71	0.72	0.82	0.89
<i>BBE_{CO}Vary</i>	0.82	0.68	0.84	0.66	1.03	0.76	1.07	0.72	1.00	0.84	1.07	0.93
<i>FFBBE_{CO}Vary</i>	0.58	0.54	0.56	0.46	0.74	0.54	0.77	0.52	0.66	0.64	0.79	0.81
<i>OH_{input}Vary</i>	0.53	0.63	0.53	0.56	0.71	0.60	0.70	0.56	0.62	0.78	0.74	0.90
<i>AllVary</i>	0.69	0.49	0.68	0.40	0.64	0.45	0.70	0.43	0.62	0.47	0.76	0.73
CO data												
<i>Base</i>	0.74	0.79	0.70	0.75	0.83	0.57	0.98	0.71	0.74	0.68	0.88	0.82
<i>E_{CH4}Vary</i>	0.74	0.79	0.70	0.75	0.82	0.57	0.98	0.71	0.73	0.68	0.87	0.82
<i>BBE_{CO}Vary</i>	0.81	0.86	0.74	0.73	0.84	0.57	1.01	0.74	0.82	0.68	0.79	0.64
<i>FFBBE_{CO}Vary</i>	0.92	0.88	0.97	0.87	0.84	0.42	0.89	0.70	0.83	0.70	0.81	0.63
<i>OH_{input}Vary</i>	0.74	0.81	0.71	0.77	0.81	0.56	0.93	0.71	0.67	0.66	0.92	0.85
<i>AllVary</i>	0.90	0.88	0.96	0.85	0.80	0.37	0.82	0.68	0.77	0.67	0.84	0.68

921 ^aGMD stations shown include Alert, Canada (ALT, 82°N, 62°W), Point Barrow, USA (BRW, 71°N, 156°W), Niwot Ridge, USA (NWR, 40°N, 105°W),
 922 Mauna Loa, Hawaii, USA (MLO, 20°N, 155°W), Ragged Point, Barbados (RPB, 13°N, 59°W), and South Pole,
 923 Antarctica (SPO, 90°S, 25°W).

924 *: "S" refers to the correlation slope (dy/dx) of the simulation/measurement comparison.

925 **: "R²" refers to the correlation coefficient.

926

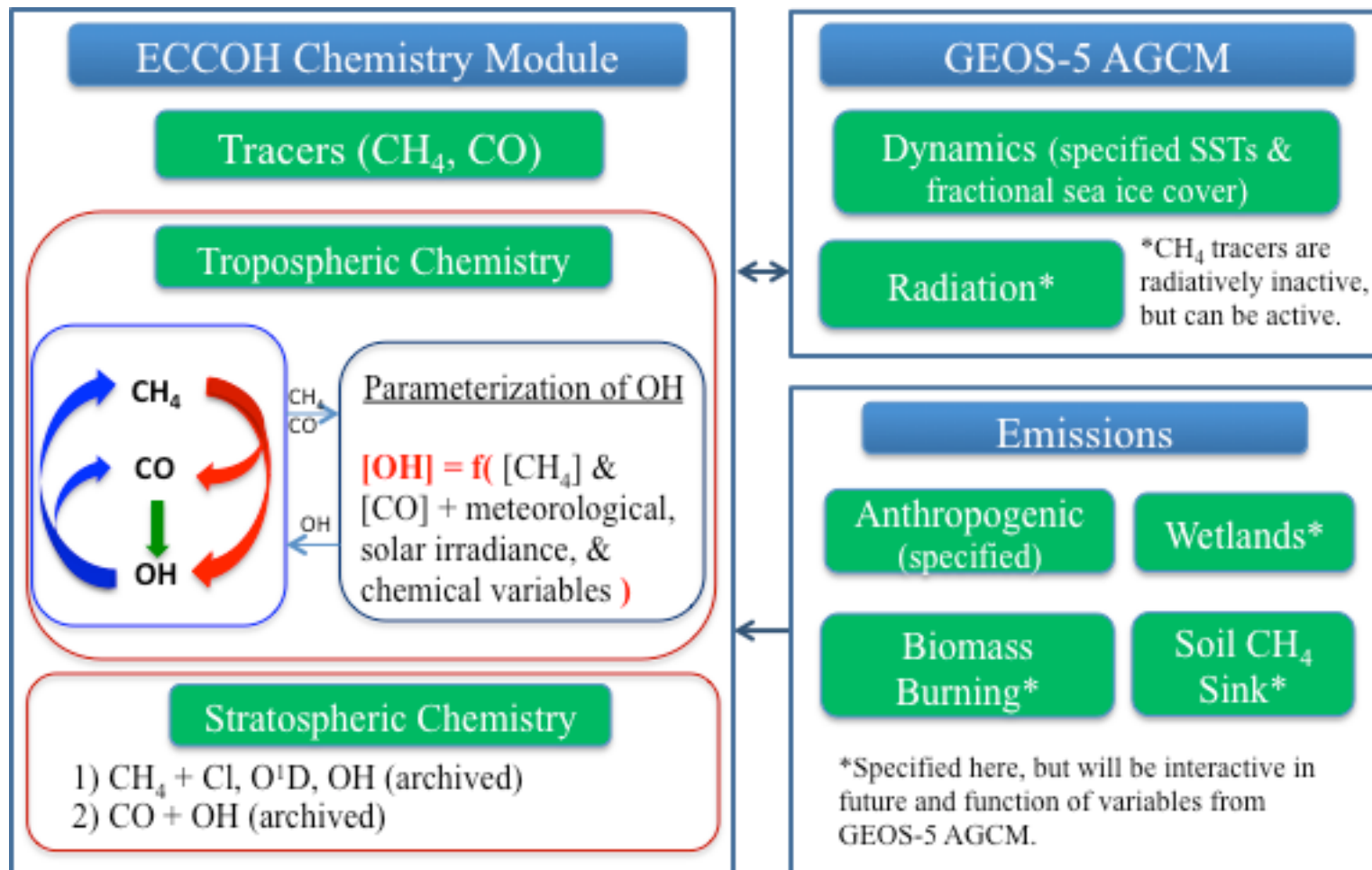


Fig. 1: Schematic representation of the implementation of the ECCOH module within the GEOS-5 AGCM.

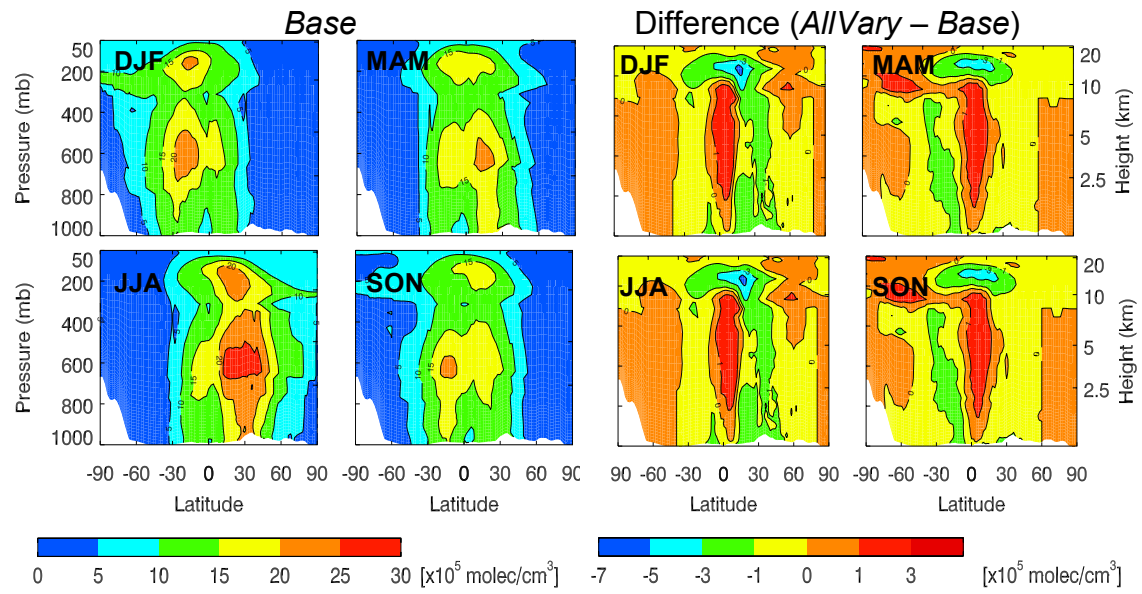


Fig. 2: Seasonal zonal mean (1988-2007) of OH ($\times 10^5$ molecules/cm³) for the *Base* scenario (left 4 panels) and the difference (*AllVary-Base*, right 4 panels) for December-February (DJF), March-May (MAM), June-August (JJA) and September-November (SON).

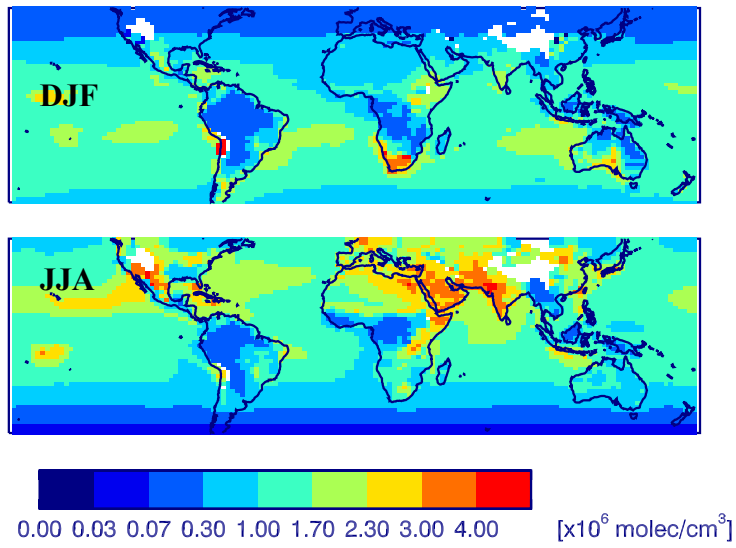


Fig. 3: Seasonal mean (1988-2007) OH ($\times 10^6$ molecules/cm³) for the *Base* scenario for December- February (DJF) and June-August (JJA) at 850 mb.

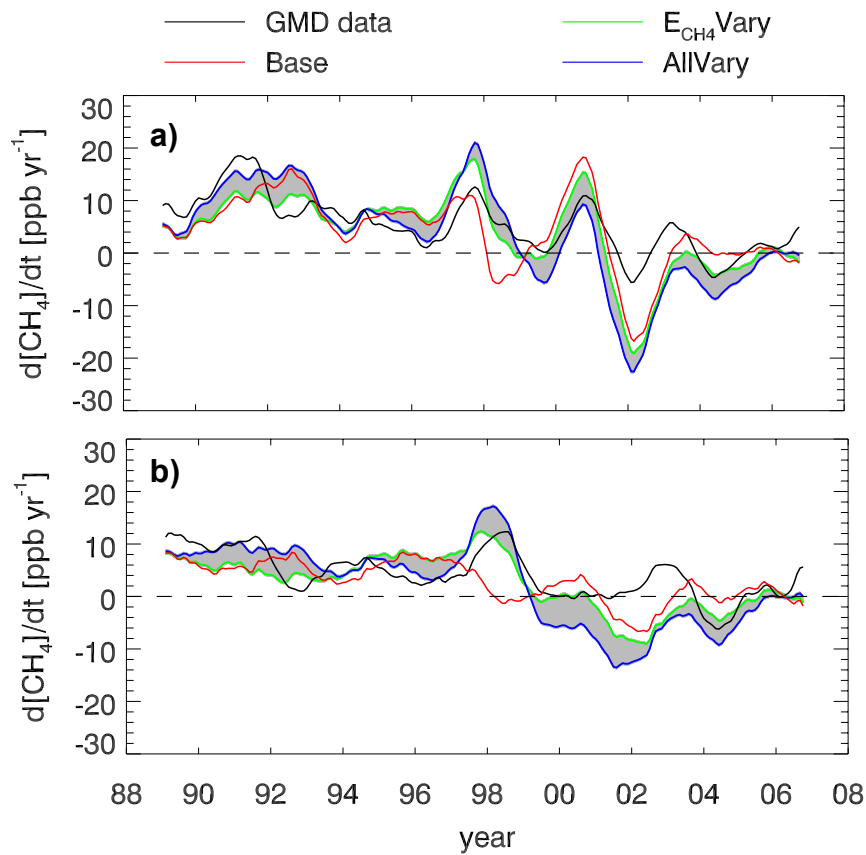


Fig. 4: a) 12-month running mean atmospheric growth rate of methane (ppbv yr⁻¹) for the average of 92 GMD stations and from model output for several scenarios averaged for those station locations. The shaded area is the difference between the E_{CH_4} Vary and AllVary scenarios, which indicates the total contribution of nonlinear feedbacks (i.e., from variations of CO emissions and variables input to the parameterization of OH) of the CH₄-CO-OH system to methane's growth rate. b) Same as a) but for the average of 17 GMD stations, which covers 100% of the simulation period. Refer to Fig. S 4 to Fig. S 7 for methane's growth rate from other scenarios.

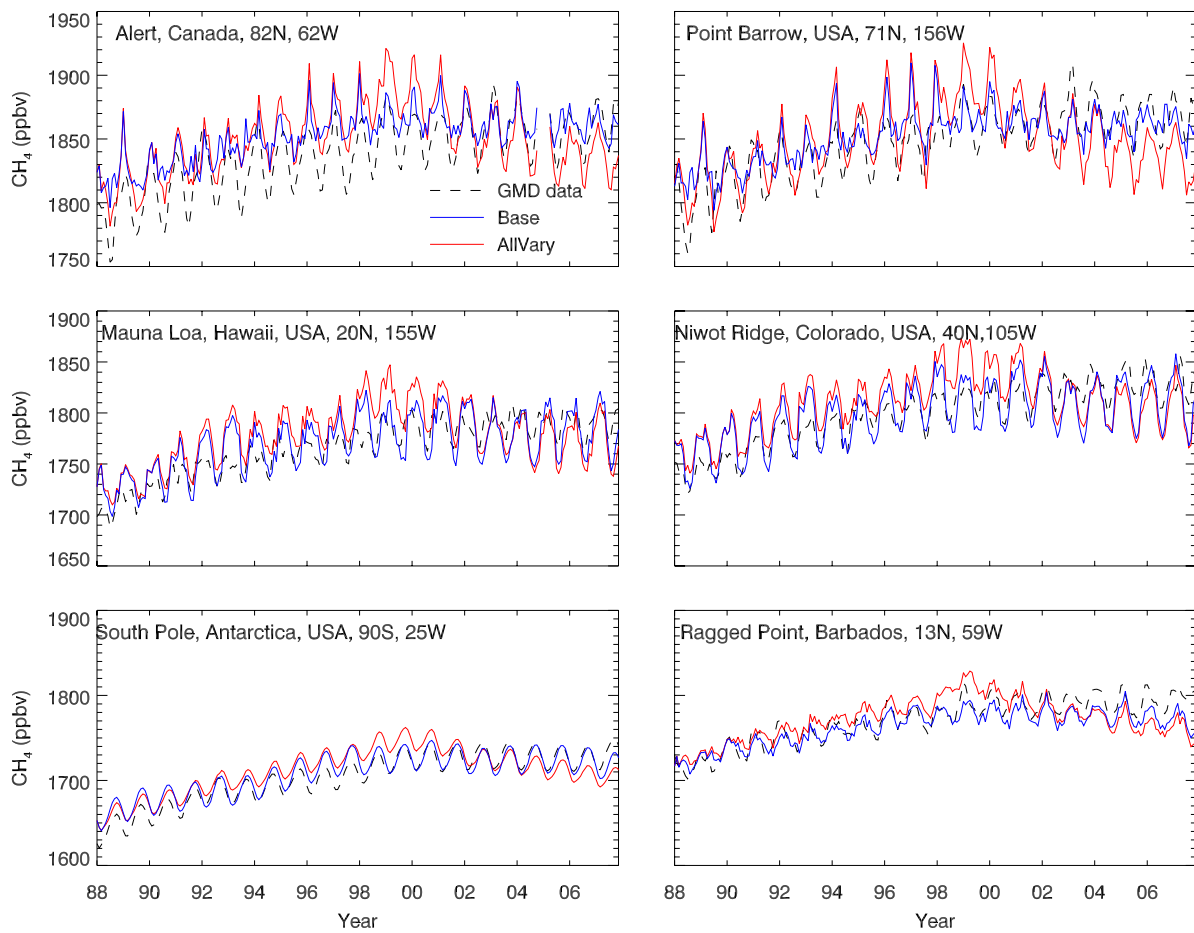


Fig. 5: Monthly methane (ppbv) from the *Base* and *AllVary* scenarios and observations from six GMD stations. Similar plots for the other scenarios are given in Fig. S 8 to Fig. S 11.

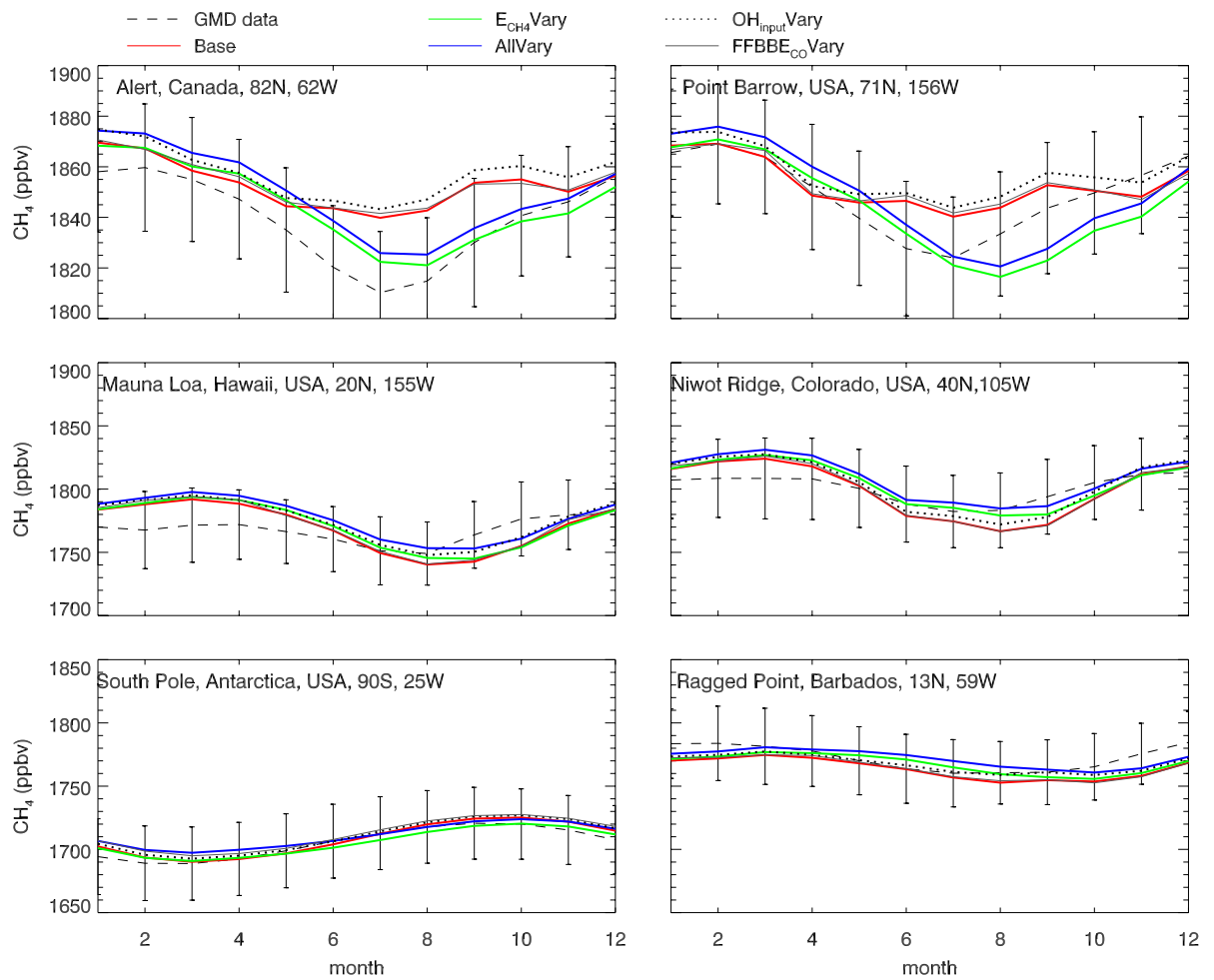


Fig. 6: Monthly methane (ppbv) averaged over 1988-2007 for several scenarios and observations at six GMD stations. Vertical lines represent the standard deviation of the observed annual mean.

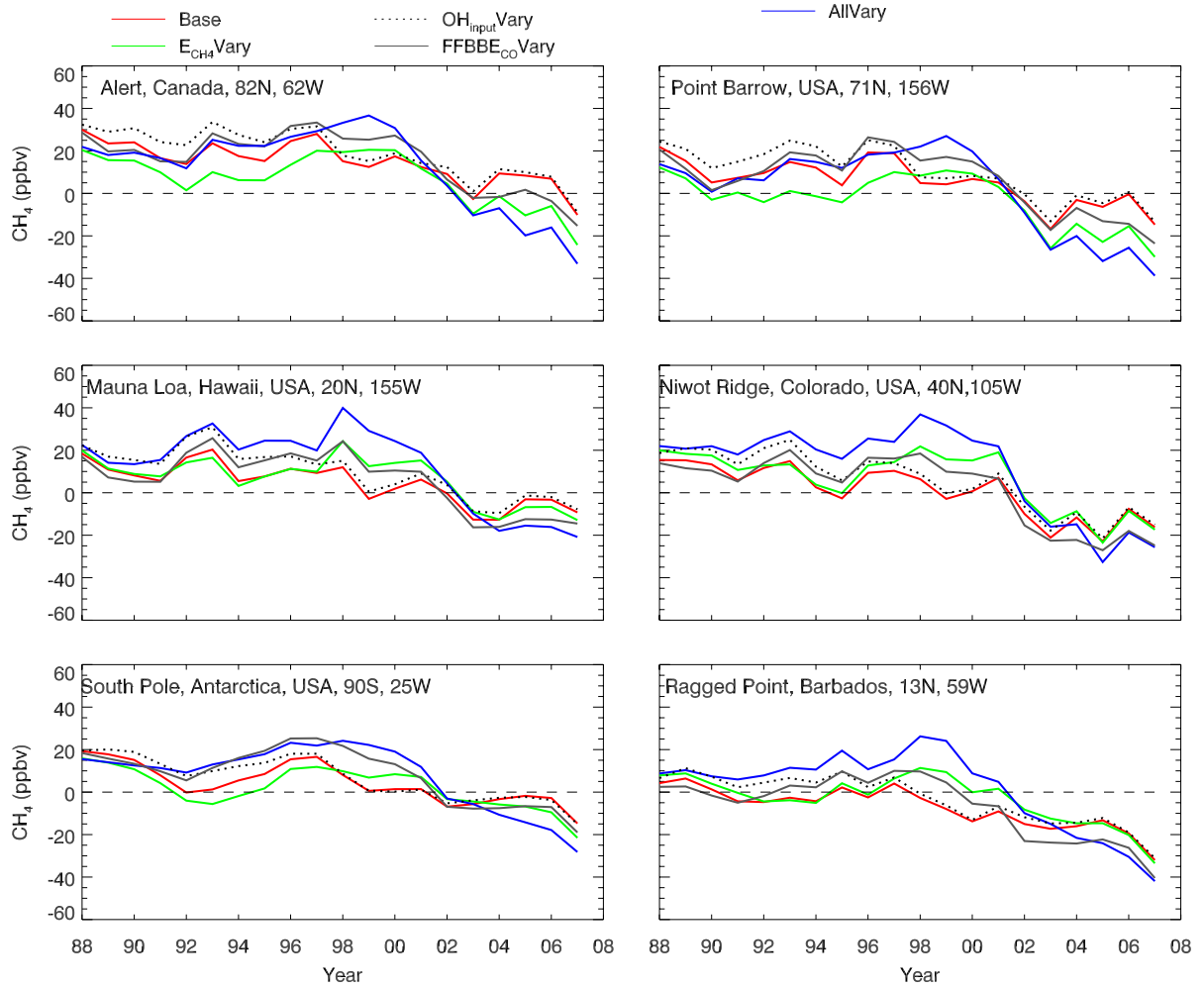


Fig. 7: Annual methane deviation (ppbv; simulated-measured) for several scenarios and observations at six GMD stations.

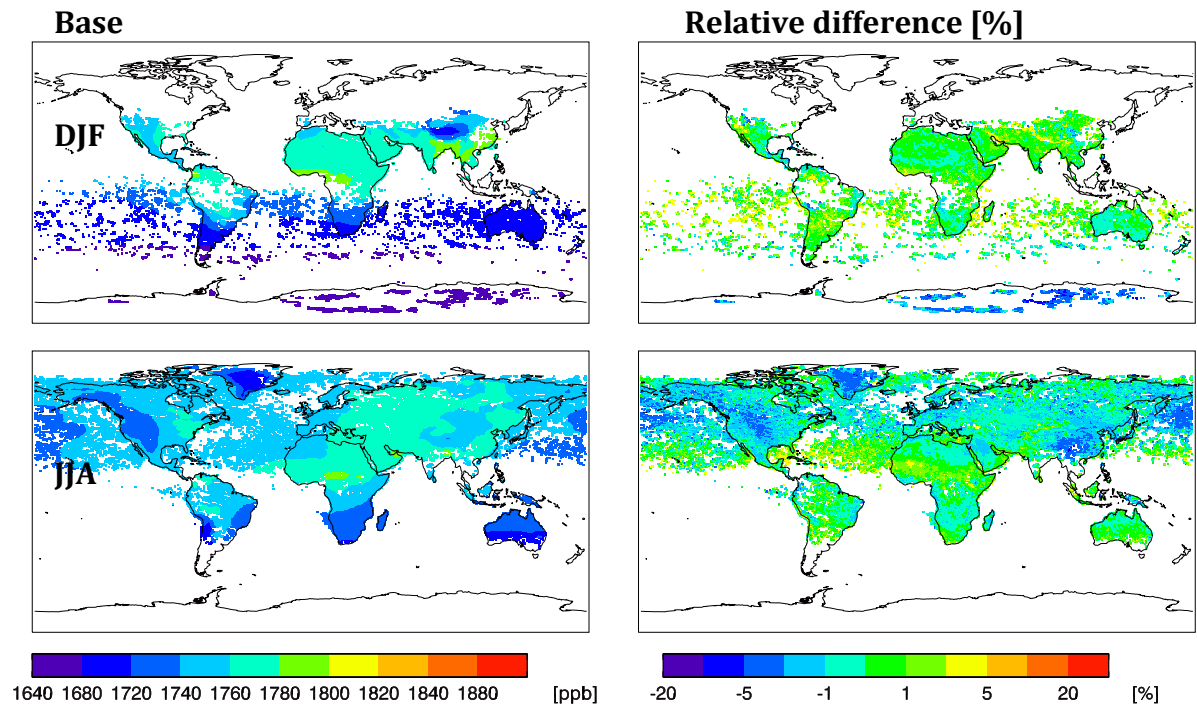


Fig. 8: Seasonal mean (2004) methane dry column (ppbv; left column) from the *Base* scenario and the relative difference (%; $(Base-observations)/observations$; right column) with SCIAMACHY data. Simulated methane levels are gridded to the spatial resolution of the SCIAMACHY data.

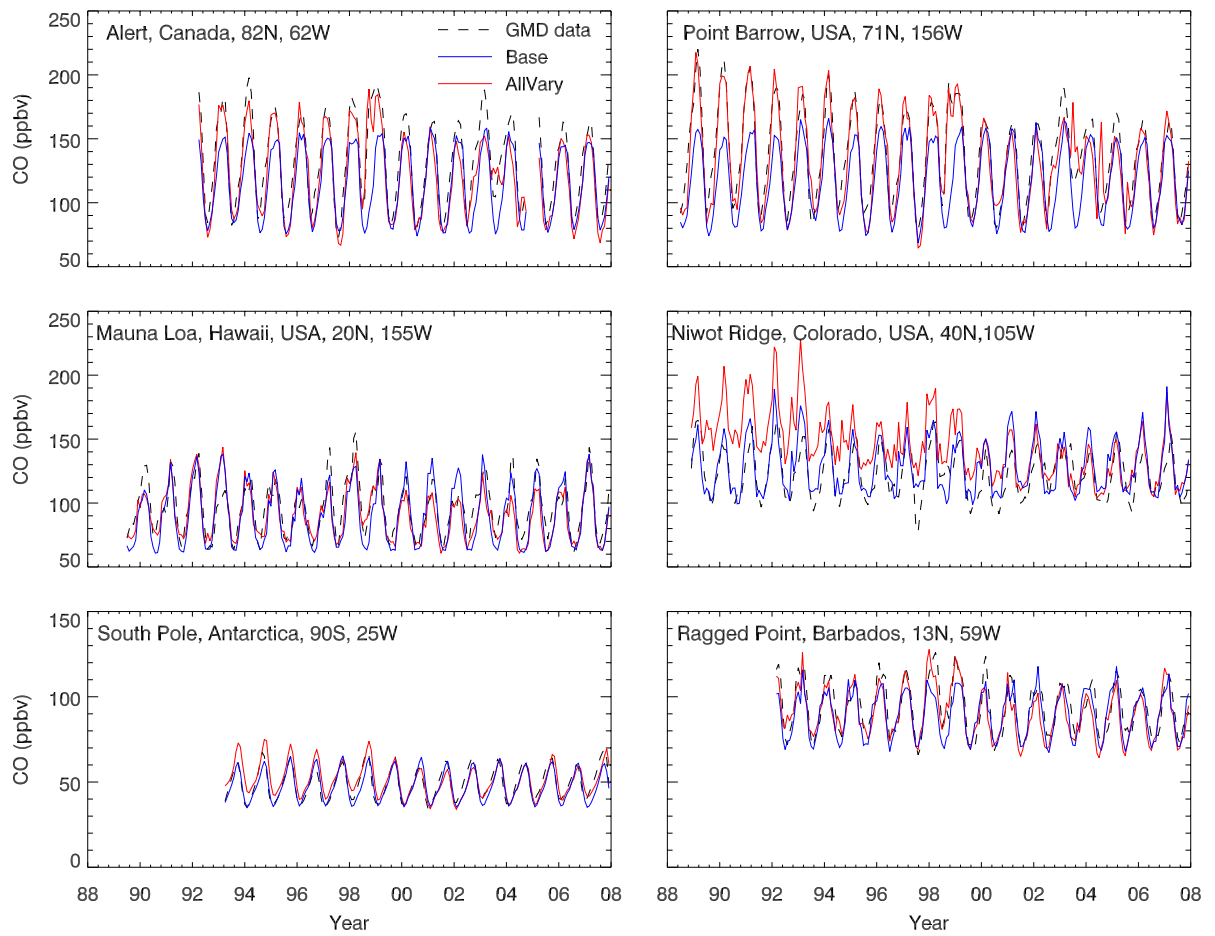


Fig. 9: Monthly CO (ppbv) from the *Base* and *AllVary* scenarios and observations from six GMD stations. Similar plots for the other scenarios are given in Fig. S13 to Fig. S16.

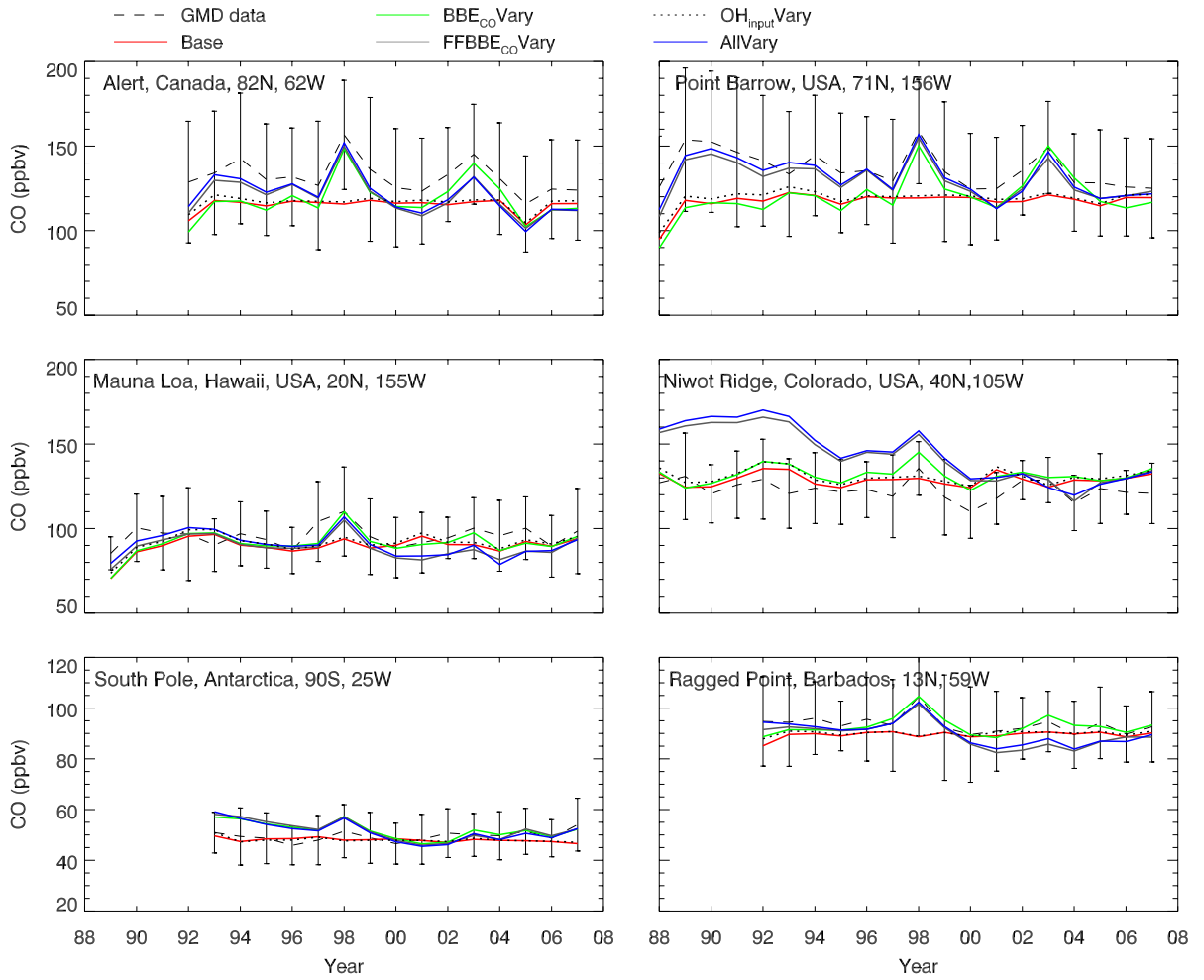


Fig. 10: Annual mean CO (ppbv) from several scenarios and observations at six GMD stations. Vertical lines represent the standard deviation of the observed annual mean.

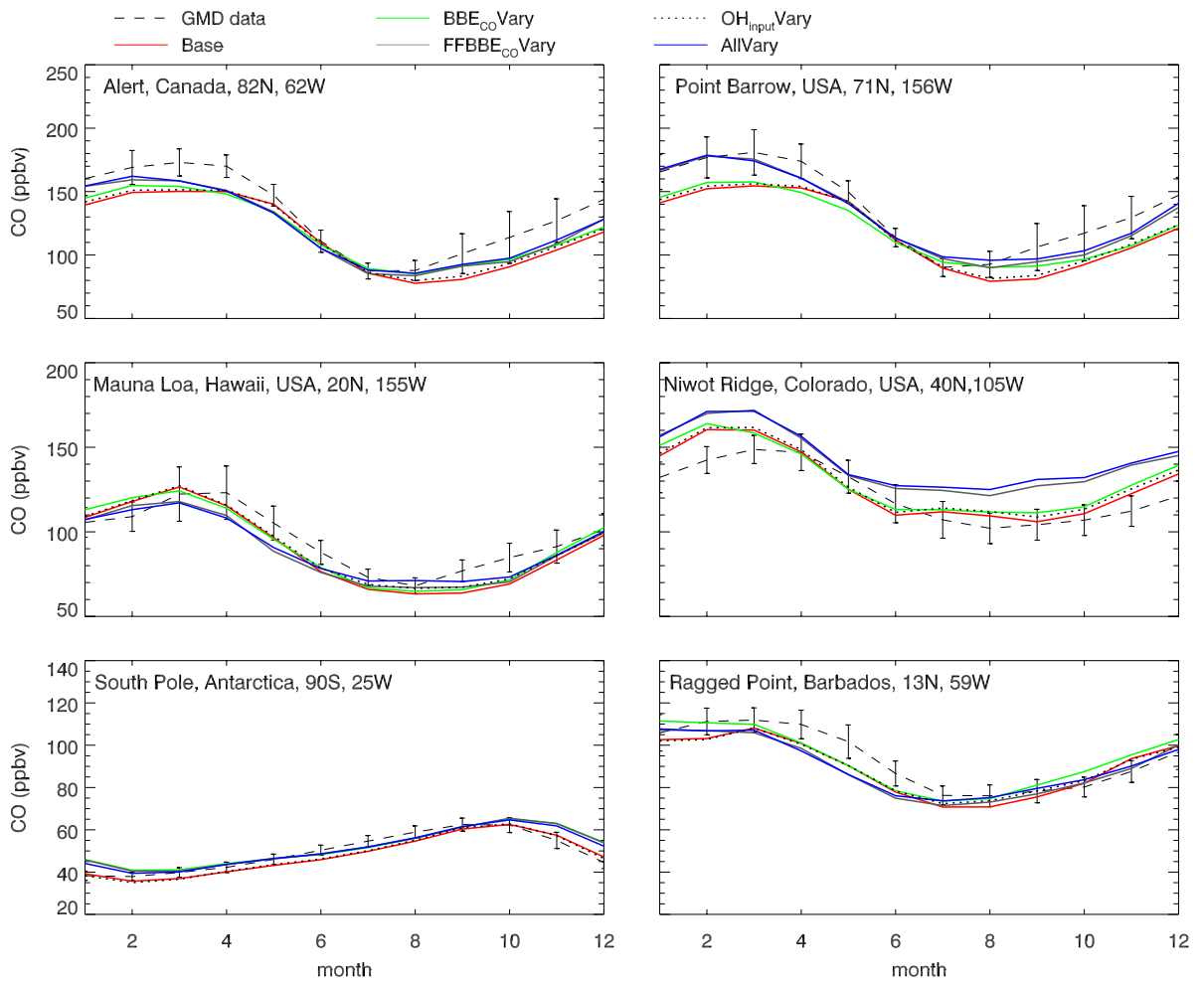


Fig. 11: Monthly CO (ppbv) averaged over 1998-2007 for several scenarios and observations at six GMD stations. Vertical lines represent the standard deviation of the observed monthly mean.

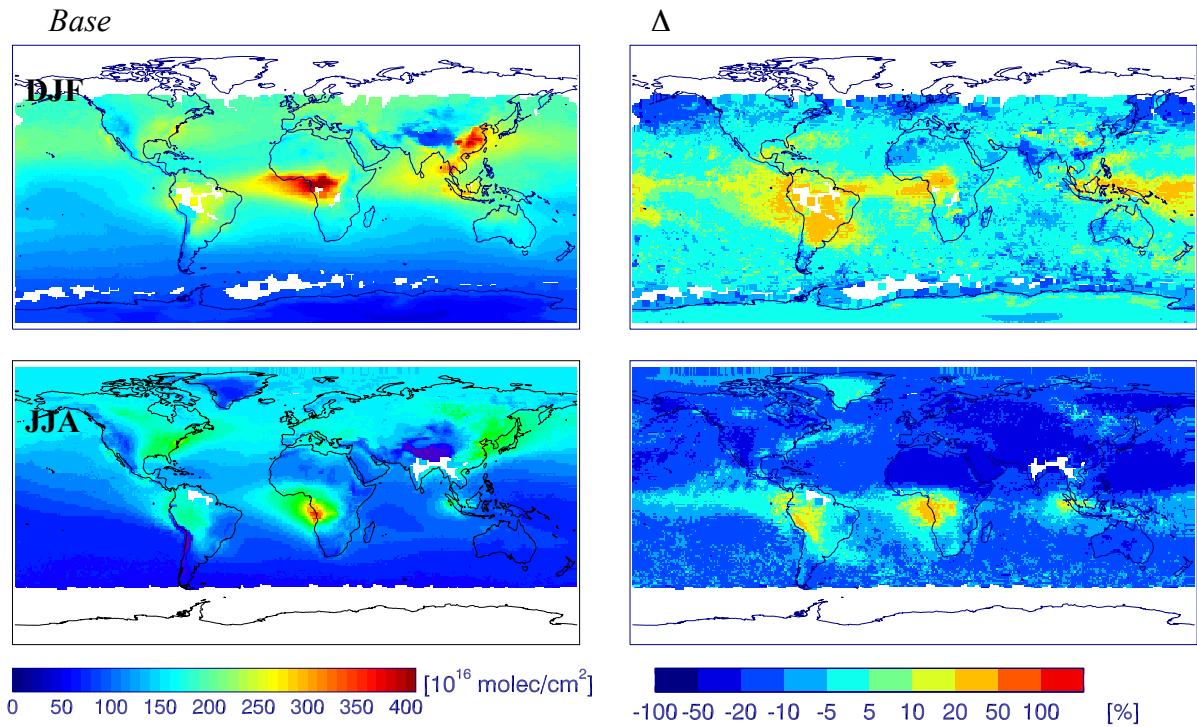


Fig. 12: Seasonal mean (2006-2007) CO columns ($\times 10^{16}$ molecules/ cm^2) from the *Base* scenario (left column) and the relative difference (%; (*Base*-observations)/observations; right column) with MOPITT data.

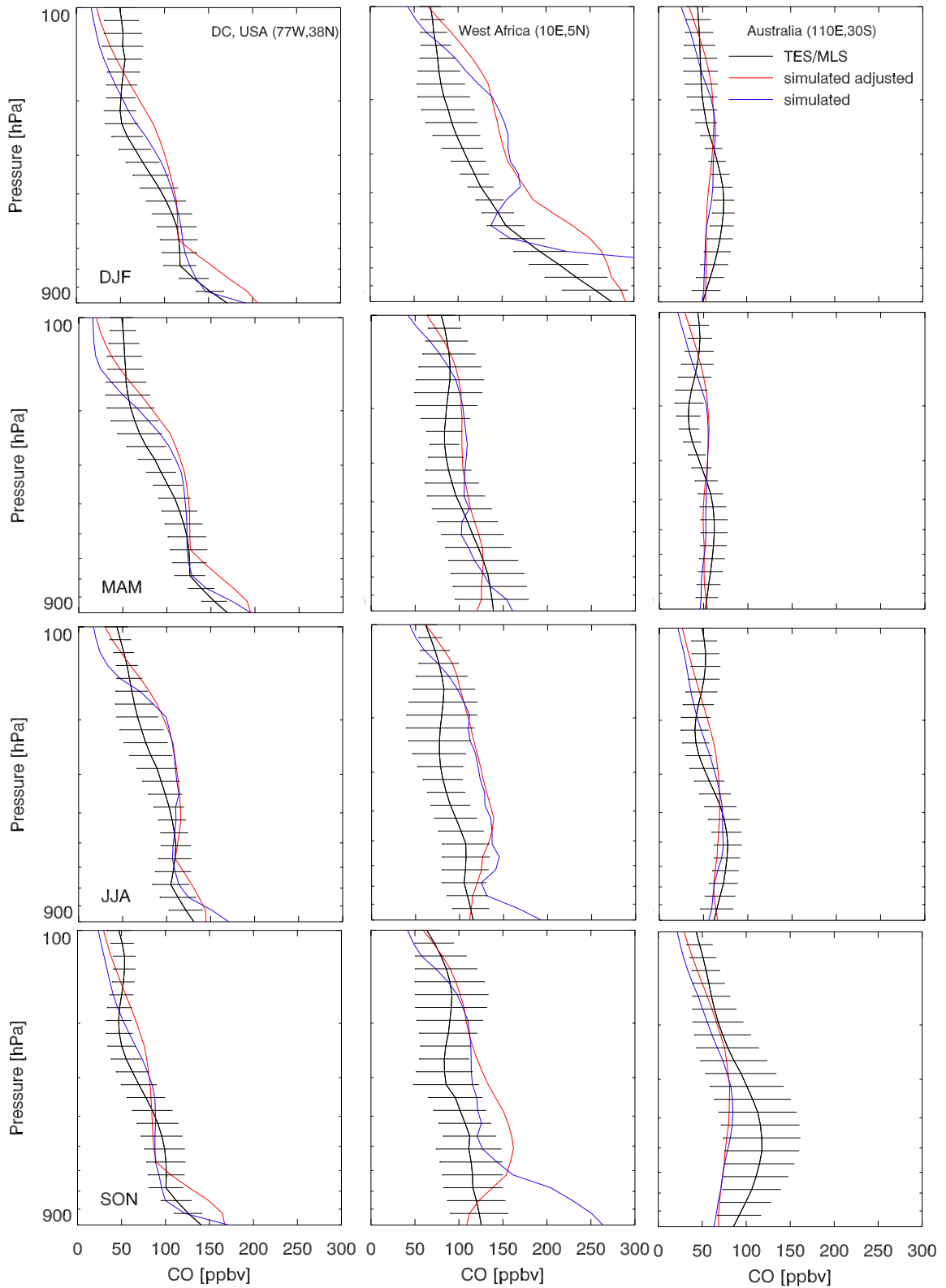


Fig. 13: Seasonal mean (2006-2007) CO vertical profiles (ppbv) over select locations of TES/MLS data, the *Base* scenario ('simulated'), and the *Base* scenario adjusted with averaging kernels ('simulated adjusted'). The horizontal bars represent the standard deviation of the individual overpasses used to create the seasonal mean.

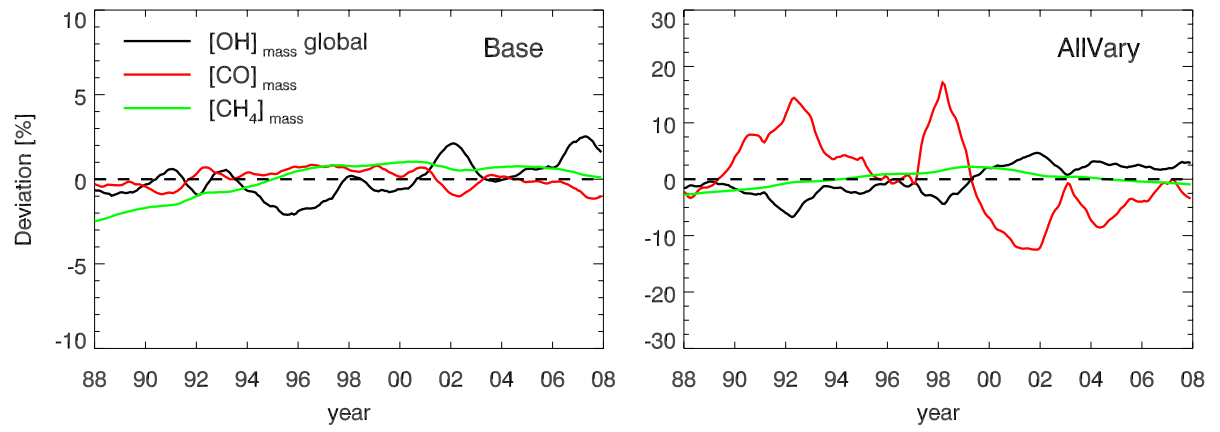


Fig. 14: Deviations of tropospheric, mass-weighted OH, CO and methane (12 month running mean) from the *Base* (left) and *AllVary* (right) scenarios. Note the different scales of the y-axes.

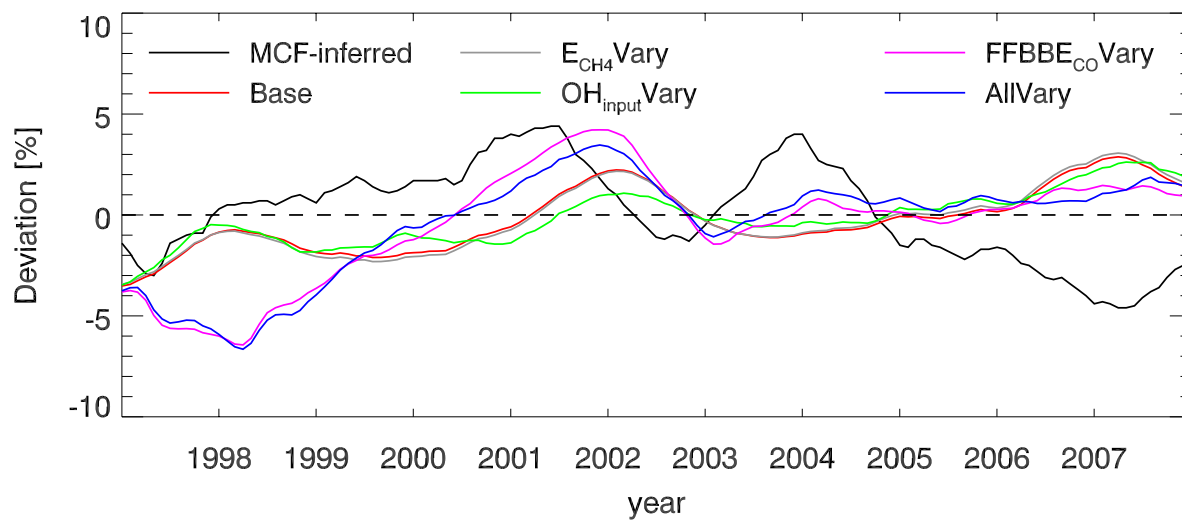


Fig. 15: Deviations (%) of the global, mass-weighted, pseudo first order rate constant (k) of the reaction of OH with MCF-inferred from MCF measurements (black; adapted from Montzka et al., 2011) and from several scenarios.

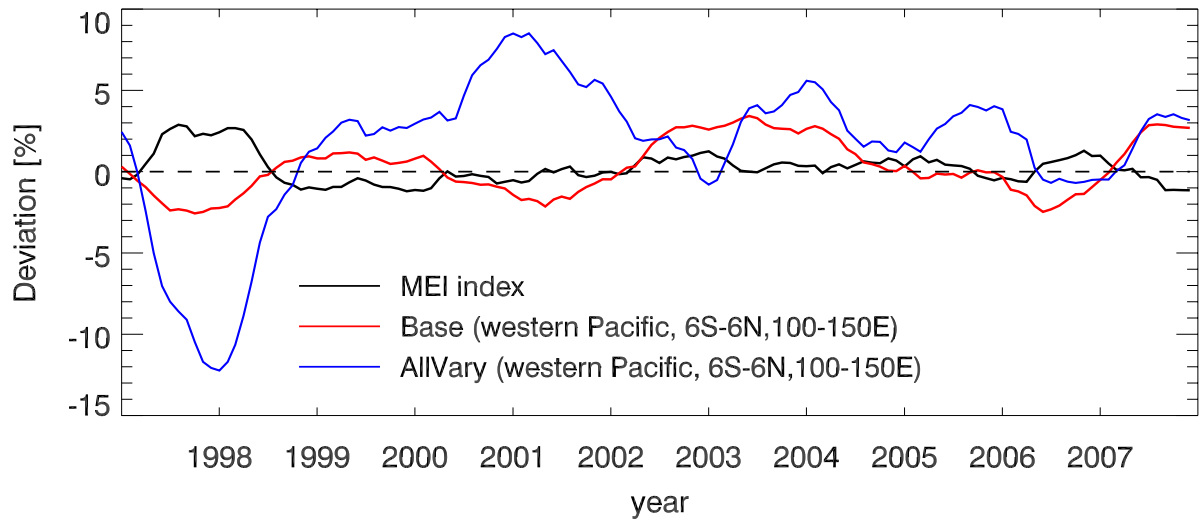


Fig. 16: Deviation (%) of global, mass-weighted OH from various scenarios and the Multivariate ENSO Index (MEI). The lines are 12-month running means. Positive values of MEI indicate El Niño conditions and negative values indicate La Niña conditions. The correlation coefficient (R^2) for the *Base* scenario vs the MEI index is 0.20 while for the *AllVary* scenario is 0.59.

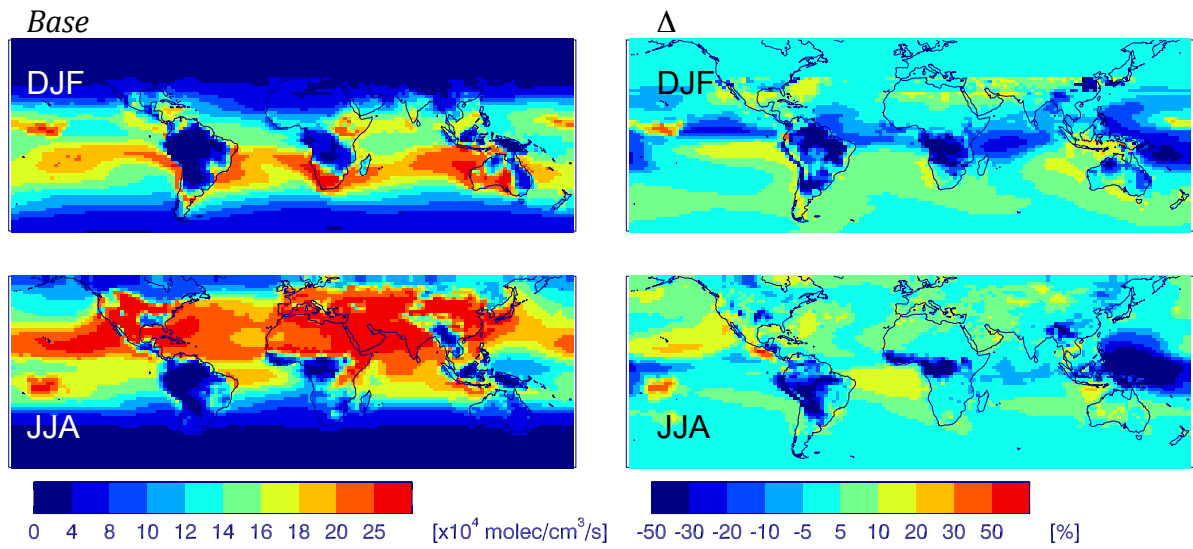


Fig. 17: Seasonal mean (1988-2007), mass-weighted tropospheric methane loss rate (left column; $\times 10^4$ molecules/cm³/s) with relative difference with the *AllVary* scenario ($(Base - AllVary)/Base$; right column).

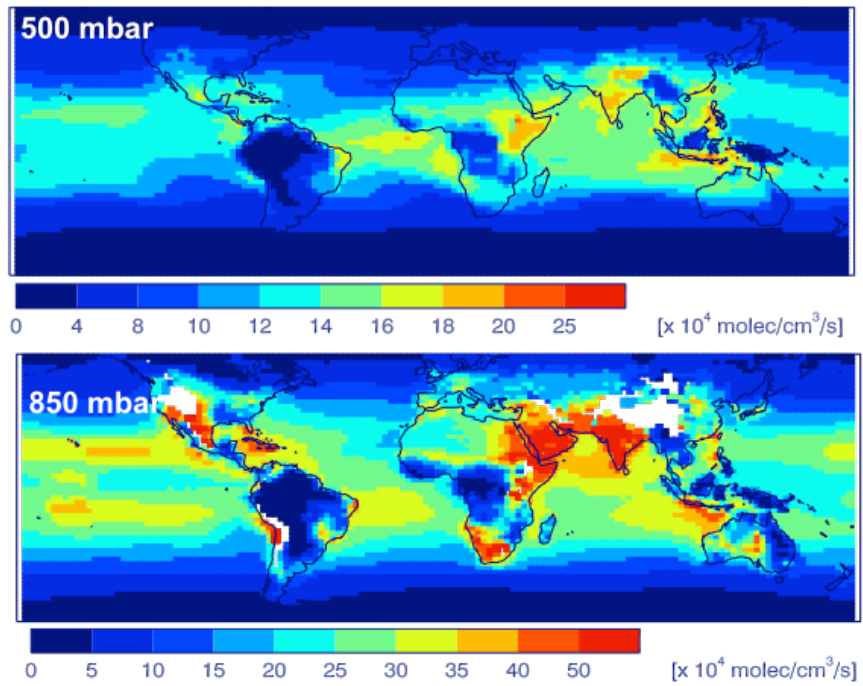


Fig. 18: Mean methane loss rate (1988-2007; $\times 10^4$ molecules/cm³/s) at 500 mb (top) and 850 mb (bottom) for the *Base* scenario.

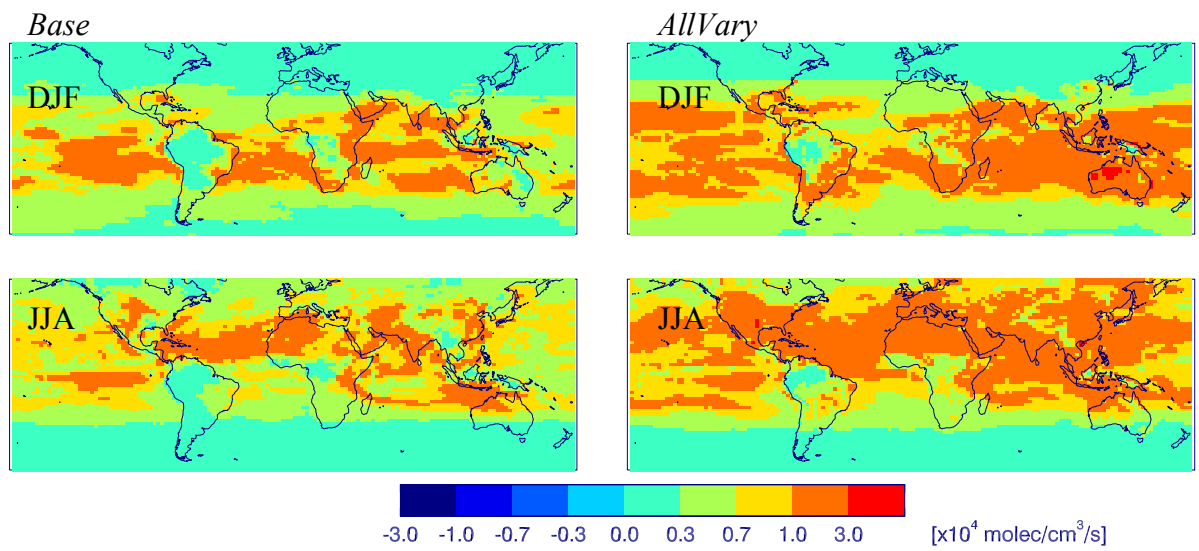


Fig. 19: Seasonal mean (1988-2007) standard deviation of tropospheric methane loss rates ($\times 10^4 \text{ molecules/cm}^3/\text{s}$) from the *Base* (left column) and *AllVary* (right column) scenarios.

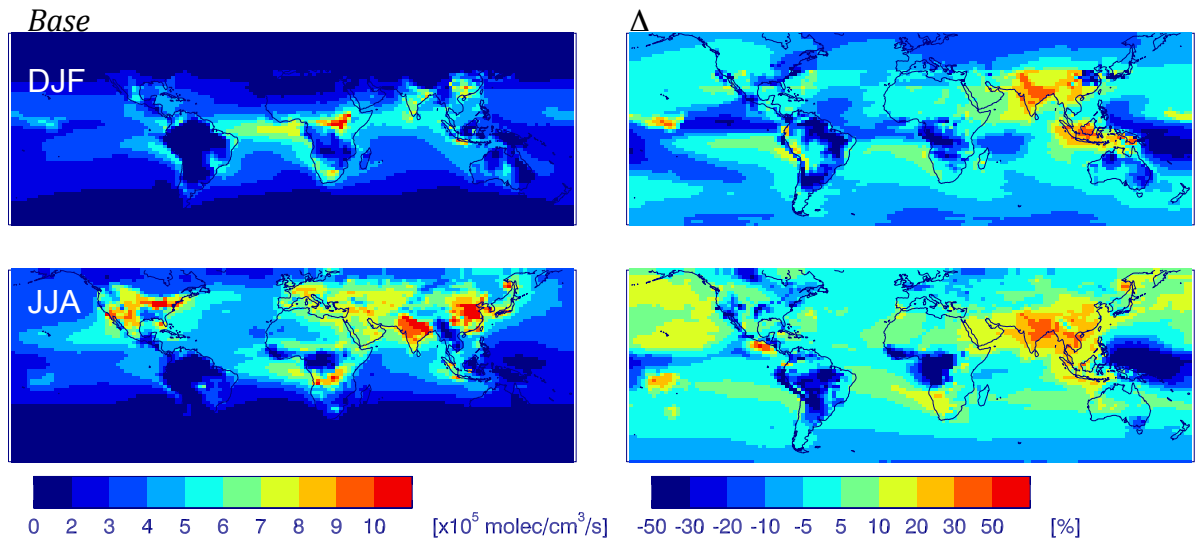


Fig. 20: Seasonal mean (1988-2007), mass-weighted tropospheric CO loss rates (left column; $\times 10^5$ molecules/cm³/s) from the *Base* scenario and relative difference (%) between the *Base* and *AllVary* scenarios ($(Base-AllVary)/Base$; right column).

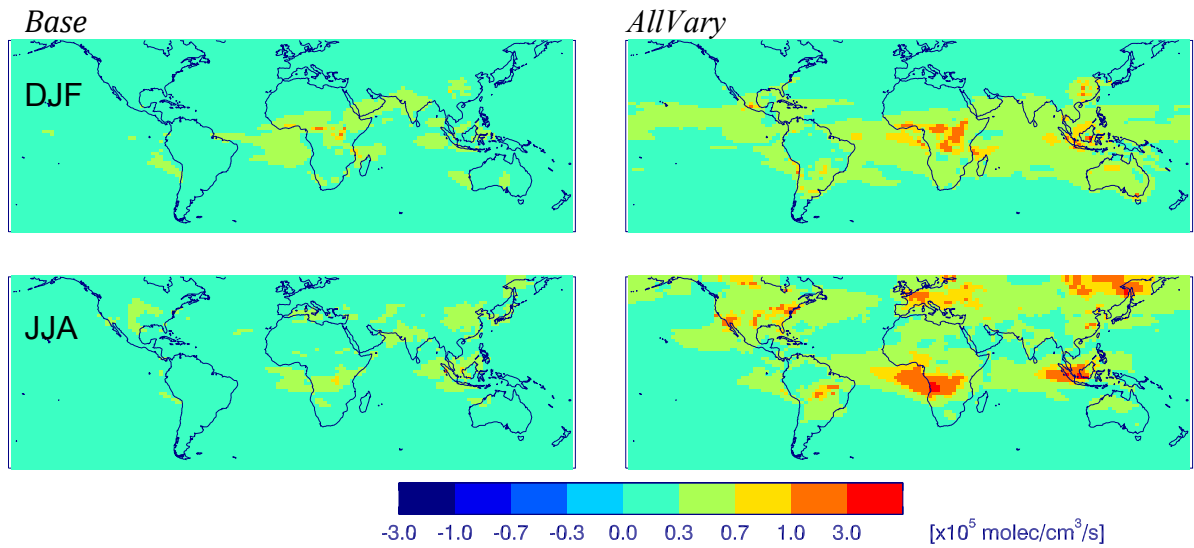


Fig. 21: Seasonal mean (1988-2007) standard deviation of tropospheric CO loss rates ($\times 10^5$ molecules/cm³/s) from the *Base* (left column) and *AllVary* (right column) scenarios.

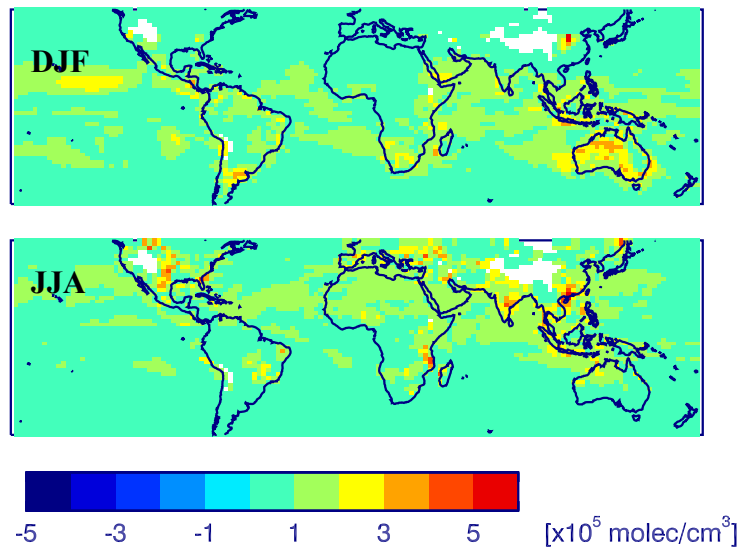


Fig. 22: Seasonal mean (1988-2007) standard deviations of OH ($\times 10^5$ molecules/cm³) at 850 mb for the *AllVary* scenario.